



Emergent phenomena and proximity effects in two-dimensional magnets and heterostructures

Bevin Huang¹  , Michael A. McGuire², Andrew F. May² , Di Xiao³ , Pablo Jarillo-Herrero⁴  and Xiaodong Xu^{1,5}  

Ultrathin van der Waals materials and their heterostructures offer a simple, yet powerful platform for discovering emergent phenomena and implementing device structures in the two-dimensional limit. The past few years has pushed this frontier to include magnetism. These advances have brought forth a new assortment of layered materials that intrinsically possess a wide variety of magnetic properties and are instrumental in integrating exchange and spin-orbit interactions into van der Waals heterostructures. This Review Article summarizes recent progress in exploring the intrinsic magnetism of atomically thin van der Waals materials, manipulation of their magnetism by tuning the interlayer coupling, and device structures for spin- and valleytronic applications.

Current technology relies on the synergy of multiple materials platforms to realize the diverse functionalities and applications that the world needs, from large-scale computing and data storage to energy-efficient lighting solutions. Van der Waals (vdW) materials provide the utility for a natural extension of this concept. Formed by layers of covalently bonded atoms that are weakly held together by vdW forces, vdW materials can be exfoliated down to the monolayer limit^{1,2}. Not only do they exhibit emergent phenomena uniquely seen in the two-dimensional (2D) limit, but also these vdW materials can be re-stacked in different combinations to form heterostructures with atomically sharp interfaces, combining or extending the properties of their constituent parts^{3,4}. This capability has led to work that includes the creation of the first atomically thin light-emitting diode⁵⁻⁷, the discovery of unconventional superconductivity in twisted bilayers of graphene⁸, and moiré-trapped valley excitons in heterobilayers of semiconducting MX₂ (refs. 9-12).

Despite over a decade of research in ultrathin/exfoliated vdW materials and their heterostructures, monolayer vdW materials with long-range magnetic order were only discovered a few years ago^{13,14}. One reason is that measuring a magnetic response in these ultrathin materials is challenging. Improvements in exfoliation and measurement techniques have allowed for such magnetism to be probed, though each characterization approach has its limits (see Box 1 for an overview of measurement techniques employed). The discovery of atomically thin magnetic vdW materials adds to what is already a diverse collection of materials platforms for studying 2D magnetism. Bulk antiferromagnetic layered perovskites, for instance, exhibit 'quasi-2D' long-range magnetic order^{15,16}, where either weak or non-interacting 2D magnetic sheets are hosted within a three-dimensional (3D) crystal lattice¹⁷. Epitaxial growth of transition metal thin films as thin as a monolayer also enabled the realization of 2D magnetism^{17,18}. Extensive study of the magnetic critical behaviour in both systems has led to experimental verifications of critical exponents derived from theoretical models of 2D spin systems^{15,18}. The magnetic anisotropy of ultrathin transition metal films has a strong dependence on the film-substrate interface, enabling the stabilization of 2D magnetism and its control by changing the film thickness or substrate¹⁸. Similarly, in magnetic oxide thin film

heterostructures, 2D magnetism at the interface can be modified by varying parameters such as octahedral tilt, chemical doping, and epitaxial strain¹⁹. For holistic reviews of these, and other 2D magnetic systems, we would like to refer readers to refs. 15-22.

Yet, there are new opportunities to explore 2D magnetism in vdW materials. These 2D flakes are suitable for device fabrication and thus the magnetic properties are susceptible to external tuning parameters such as electrostatic gating and fields²³⁻²⁵, pressure^{26,27} and strain²⁸. We would like to refer readers to reviews of the electrical control of the 2D magnetic order along with applications in magnetic tunnel junctions via spin filtering effects²⁹⁻³¹ in refs. 23-25. Their universal compatibility with other vdW materials also enables flexible heterostructure design without lattice-matching constraints^{3,24,32}. This can be leveraged to realize new spin^{24,33-35} and valleytronics^{36,37} devices, and investigate the interplay between magnetism, topology and other many-body phases^{38,39}. We refer readers to ref. 17 for an in-depth review comparing the magnetism in vdW materials with other 2D magnetic systems.

In the following Review, we highlight some of the new aspects and opportunities offered by magnetic vdW materials tabulated in Table 1 and their heterostructures. We present a brief overview of the relevant structural and magnetic properties in the bulk crystal form for each material, followed by a summary of the work that has been done in the mono- and few-layer limit. Then, we discuss the work on the correlation between magnetic order and layer stacking arrangement, and its control via hydrostatic pressure. Lastly, we detail the progress of incorporating these magnetically active materials into heterostructures for spin- and valleytronics applications and provide an outlook on future directions for the field of magnetic vdW materials.

Chalcogen-based vdW magnets in the atomically thin limit

Chalcogen-based vdW materials form a large fraction of the systems where long-range magnetic order has been experimentally demonstrated at the time of writing this Review. This class of materials exhibits a diverse array of magnetic phenomena, including antiferromagnetic insulators with varying degrees of anisotropy^{28,40-51}, ferromagnetism at room temperature⁵²⁻⁵⁴, and topologically non-trivial antiferromagnetic insulators^{38,39,55-60}. In this section, we highlight

¹Department of Physics, University of Washington, Seattle, WA, USA. ²Materials Science and Technology Division, Oak Ridge National Laboratory, Oak Ridge, TN, USA. ³Department of Physics, Carnegie Mellon University, Pittsburgh, PA, USA. ⁴Department of Physics, Massachusetts Institute of Technology, Cambridge, MA, USA. ⁵Department of Materials Science and Engineering, University of Washington, Seattle, WA, USA. ✉e-mail: huangbev@uw.edu; xuxd@uw.edu

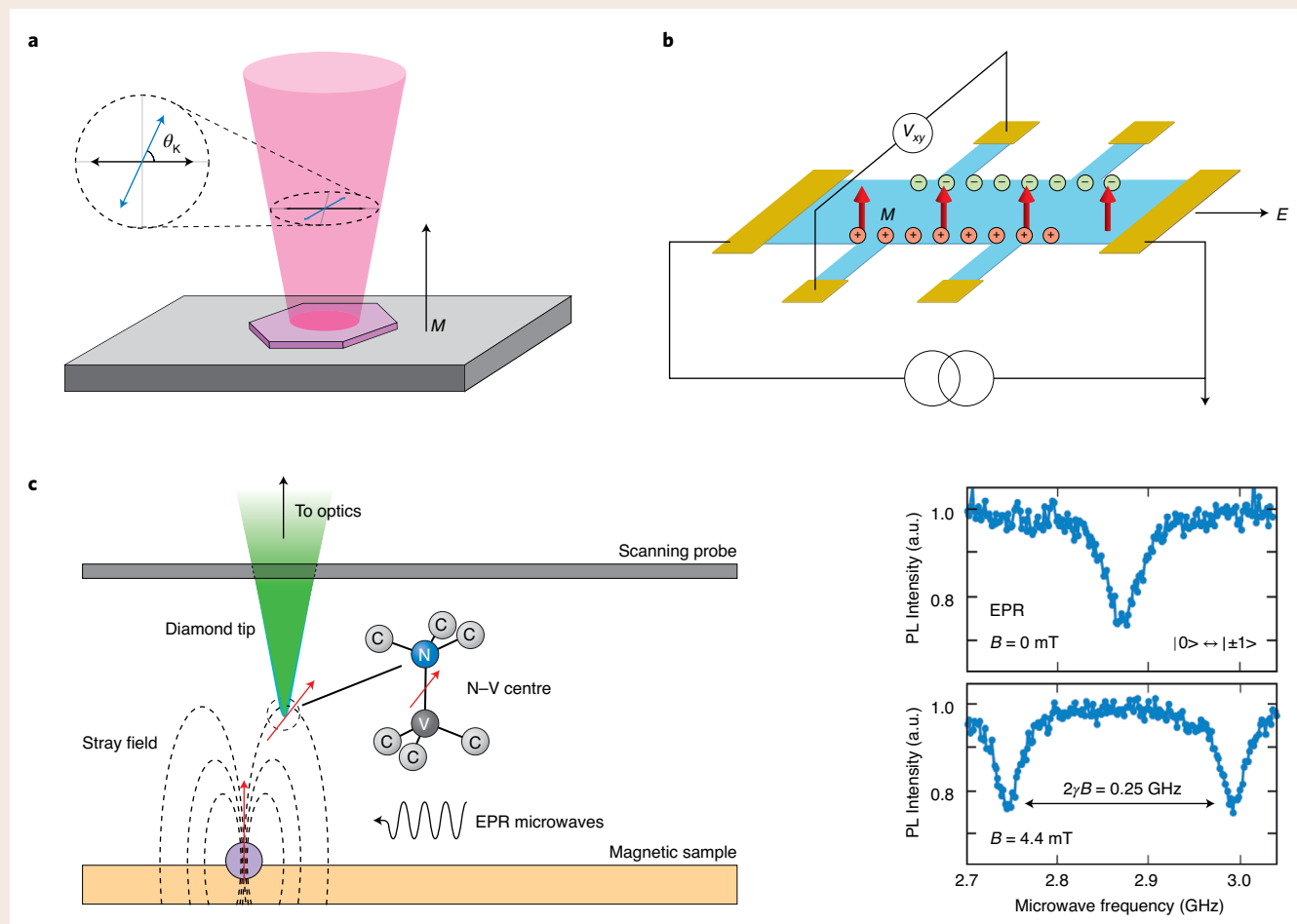
Box 1 | Characterization methods for ultrathin magnetic vdW materials

Determining the magnetic state of ultrathin magnetic vdW materials, particularly of antiferromagnetic order, is an ongoing challenge since their minuscule magnetic moments and air sensitivity render conventional magnetic probes such as neutron diffraction, X-ray magnetic circular dichroism spectroscopy, and SQUID magnetometry ineffective. While there has been progress using optical and electrical probes to study the magnetic properties of vdW materials down to the monolayer limit, each technique has its own advantages and drawbacks. Furthermore, none of these probes directly measure the magnetization—they cannot directly

determine the magnetic state of a material on their own. Some of these probes include the following.

Polar magneto-optical Kerr effect (MOKE)

A magneto-optical technique where linearly polarized light normally reflected off an out-of-plane magnetized sample undergoes a rotation of its linear polarization due to magnetic circular birefringence (panel **a** of Box figure). This rotation, θ_K , depends on the out-of-plane magnetization of the material, the substrate, and the excitation wavelength used^{13,23}. The backscattering geometry used to focus and collect light from these



Schematics of measurement techniques for ultrathin magnetic vdW materials. **a**, Illustration of polar MOKE microscopy. Linearly polarized light incident (black double-sided arrow in left inset) on a sample (purple hexagon) with out-of-plane magnetization, M , is reflected with some Kerr rotation, θ_K , of its linear polarization (blue double-sided arrow of left inset). **b**, Schematic of a typical Hall bar device used to probe the anomalous Hall effect in ultrathin magnetic vdW materials. Conduction electrons in an itinerant ferromagnet that are spin-polarized out-of-plane pick up an anomalous velocity that is perpendicular to a bias electric field, E , from spin-dependent scattering and non-zero Berry curvature. This sets up a transverse electric potential, V_{xy} , which is proportional to the averaged out-of-plane magnetization, M , in the sample region contained by the Hall bar. **c**, Overview of NV centre magnetometry. A NV centre localized near the surface of a diamond tip can be used as a point-like single spin sensor to map out the stray magnetic fields of an underlying sample (left panel). The intensity of photoluminescence (PL) generated from the NV centre ground state is dependent on the initial $S = 1$ electron spin state ($|0\rangle$ or $|\pm 1\rangle$), with stronger PL emission from the $|0\rangle$ state due to non-radiative relaxation pathways in the $|\pm 1\rangle$ excited states. Crystal field splitting of ~ 2.87 GHz between the $|0\rangle$ and $|\pm 1\rangle$ ground states allows for selective microwave pumping of electrons to the $|\pm 1\rangle$ ground states through electron paramagnetic resonance (EPR). This is observed as a dip in the PL intensity when the microwave frequency is resonant with the EPR (upper-right panel). With the addition of a small magnetic field, B , such as the stray fields from a magnetic sample, Zeeman splitting of the $|1\rangle$ and $|-1\rangle$ ground states leads to two dips with a difference frequency, $2\gamma B$, where γ is the gyromagnetic ratio of the electron in the NV centre, which is roughly 25.8 MHz mT^{-1} (lower-right panel). At a magnetic field of 4.4 mT, the $|1\rangle$ and $|-1\rangle$ ground states are split by ~ 250 MHz. Panel **c** adapted with permission from: ref. ¹³⁵, Annual Reviews; ref. ¹³⁶, AIP; and ref. ¹³⁷, Springer Nature Ltd.

Continue

Box 1 | Characterization methods for ultrathin magnetic vdW materials (Continued)

microscopic samples and the requirement of a net magnetization limits MOKE and reflective magnetic circular dichroism (RMCD) microscopy, a closely related magneto-optical technique, to probing out-of-plane ferromagnetic or ferrimagnetic order. Antiferromagnetic order can be indirectly inferred if spin-flop or spin-flip transitions occur as an external magnetic field is swept^{13,38}. However, such magnetization reversal behaviour could also be mistaken for nanoscopic domain dynamics^{18,73,112} that cannot be spatially resolved by a micrometre-sized beam spot. The different types of antiferromagnetism (zigzag, Néel, stripy) also cannot be determined.

Anomalous Hall measurements

For itinerant ferromagnets, the free carriers themselves are spin-polarized. When measuring the electrical transport of such a ferromagnet (panel **b** of Box figure) in an externally applied magnetic field, $\mu_0 H$, its total Hall resistance, R_{xy} , will take the form, $R_{xy} = R_0 \mu_0 H + R_A M$, where the first term is the magnetic field-dependent ordinary Hall effect and the second term is the anomalous Hall contribution where M is the averaged magnetization across the entire device area. Anomalous Hall measurements, however, require a conductive sample, and the fabrication process to make electrical contact to most ultrathin magnetic vdW materials is difficult due to their air sensitivity. A sample-averaged net out-of-plane magnetization is required, and spatial mapping of domains is not possible.

Raman spectroscopy and second harmonic generation (SHG)

Optical techniques that detect the effects of magnetic ordering on the Γ -point quasiparticle spectrum in Raman spectroscopy^{50,51,62}, and $|\chi^{(2)}|$ for SHG¹¹⁰. These techniques are useful for detecting magnetic behaviour that would otherwise be inaccessible through polar MOKE and RMCD microscopy like antiferromagnets and ferromagnets with easy-plane anisotropy^{31,41,110}. For instance, analysis of the polarization dependence and peak splitting of phonon modes can reveal magnetism-induced symmetry breaking^{41,133} (see the section ‘Chalcogen-based vdW magnets in the atomically thin limit’ for specific examples with the XPS₃ system). Such symmetry breaking can also enable giant SHG¹¹⁰. However, these optical techniques will not detect magnetic order in the absence of strong spin-phonon coupling that leaves

signatures in polarization-dependent Raman measurements, or symmetry-breaking that enables both SHG and the activation of Raman modes.

There has also been development of nanoscale magnetic imaging techniques such as magnetic force microscopy (MFM)⁷³, nitrogen-vacancy (NV) centre magnetometry¹⁰⁹, and spin-polarized scanning tunnelling microscopy (STM)¹¹⁹ for use in ultrathin magnetic vdW materials. In MFM, the stray magnetic field gradient is measured through changes in the tapping frequency of a magnetically coated tip. It is difficult to infer the magnetization of the sample from these measurements. For NV centre magnetometry, stray fields from the magnetic sample (panel **c** of Box figure, left) induce Zeeman splitting of the spin-split NV centre orbital ground states, $|s = 0\rangle$ and $|s = \pm 1\rangle$ (panel **c** of Box figure, right). These stray field scans are backwards propagated to form images of the sample magnetization¹⁰⁹ that can be used to identify whether a sample is a ferromagnet, ferrimagnet or an A-type antiferromagnet. The spatial resolution of both these nanoscale imaging techniques can reach ~ 10 nm, useful for studying nanoscopic domains and magnetic textures. However, both techniques cannot probe materials with zigzag, stripy and Néel antiferromagnetic order since the resulting stray magnetic field is zero.

Spin-polarized STM maps the tunnelling current through ultrathin magnetic samples using an atomically sharp magnetic tip (of chromium or iron, for example), allowing for spatial maps of antiferromagnetic and ferrimagnetic order, nanoscopic domains, and magnetic textures with atomic resolution¹³⁴. As such, the adaptation of spin-polarized STM to characterize ultrathin magnetic vdW materials would be indispensable as it would be the only direct probe of zigzag, stripy and Néel antiferromagnetic order. However, a substantial challenge that needs to be addressed is sample preparation. Ultrathin vdW flakes and heterostructures prepared through commonly used exfoliation and transfer techniques leave polymer residue that can only be removed through hot annealing. Since a majority of ultrathin magnetic vdW materials are volatile at high temperatures, this annealing process may lead to sample degradation. An alternate approach is to grow monolayer materials via molecular beam epitaxy¹¹⁹, though the choice of materials that can be grown is limited.

the recent work on these chalcogenides focusing primarily on their properties in the atomically thin limit.

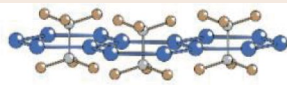
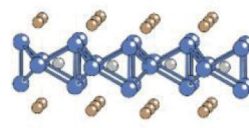
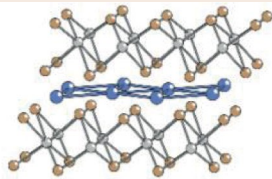
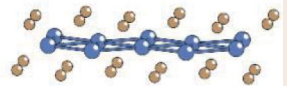
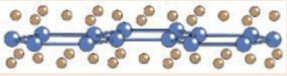
XPS₃ (X = Fe, Ni, Mn). In the bulk form, the transition metal phosphorus trisulfide compounds (thiophosphates), XPS₃ (X = Fe, Ni, Mn) are isostructural insulators that exhibit antiferromagnetic order below Néel temperatures (T_N) of 118 K in FePS₃ (refs. 40,44–46), 155 K in NiPS₃ (ref. 47) and 78 K in MnPS₃ (ref. 48). Within each layer, the magnetic ions form a honeycomb lattice penetrated by (P₂S₆)⁴⁻ complex anions (Table 1). The magnetic coupling is through superexchange pathways involving one sulfur atom in nearest neighbour interactions (J_1) and two sulfur atoms in next-nearest (J_2) and next-next-nearest neighbour interactions (J_3)²⁸. The ratios of J_1 , J_2 and J_3 , along with the orbital occupancy of the transition metal cation⁴⁸, are crucial for determining the magnetic order in the XPS₃ system. This results in diverse magnetic states of zigzag antiferromagnetism in FePS₃ and NiPS₃, and Néel antiferromagnetism in MnPS₃. Their magnetic anisotropies also vary substantially, with FePS₃ being uniaxial with the largest out-of-plane anisotropy of 2.66 meV, NiPS₃ having approximate easy-plane anisotropy characterized by a weaker anisotropy of 0.3 meV and slight preference for spins to align along the zigzag

chain direction, and MnPS₃ being virtually isotropic with an anisotropy of 0.0086 meV (ref. 49).

One method to detect magnetic order in ultrathin materials, especially of antiferromagnetic order, is Raman spectroscopy, an inelastic light scattering microscopy technique that can probe quasiparticle excitations such as phonons and magnons (see Box 1 for advantages and shortcomings of Raman spectroscopy). As seen in Fig. 1a, a set of four peaks appear in the Raman spectrum of bulk FePS₃ when cooled below T_N (refs. 50,51). The highest energy mode of the four at 10 K is a pair of degenerate antiferromagnetic magnons⁵¹, while the three lowest energy peaks are M-point phonons that are folded onto the Γ point due to zigzag antiferromagnetic order doubling the size of the unit cell^{50,51}. These phonon modes are present even in monolayer FePS₃, providing evidence for zigzag antiferromagnetic order in the monolayer limit with T_N equal to that of bulk.

In bulk NiPS₃, a Raman signature of in-plane zigzag antiferromagnetic order is the splitting of a twofold-degenerate E_g phonon mode at 180 cm⁻¹ (P_2) into an A_g mode and a B_g mode below T_N (Fig. 1b)⁴¹. This splitting persists down to bilayers and originates from differences in how the Ni sites vibrate between the two modes, along (B_g) versus orthogonal (A_g) to the easy/zigzag axis⁴¹. In MnPS₃, with Néel type antiferromagnetic order, the appearance of a new

Table 1 | Magnetic properties and crystal structures of vdW magnets discussed in this Review

Material	Magnetic Order	T_C/T_N (K)	Bandgap ^b (eV)	Additional notes	Crystal structure
FePS ₃	AFM [⊥]	118	1.6	Zigzag	MAX ₃ 
NiPS ₃	AFM	148 ^a –166 ^b	1.7	Zigzag, slight tilt out-of-plane	
MnPS ₃	AFM	78	3.0	Neél, isotropic	
CrGeTe ₃	FM [⊥]	<5 ^a –61 ^b	0.38		Fe ₃ GeTe ₂ 
Fe ₃ GeTe ₂	FM [⊥]	70 ^a –221 ^b	Metallic		
Fe ₂ GeTe ₂	FM [⊥]	270 ^a –310 ^b	Metallic		
MnBi ₂ Te ₄	L-AFM [⊥]	21	0.1	Intrinsic magnetic topological insulator L-AFM: intralayer FM, interlayer AFM	MnBi ₂ Te ₄ 
VSe ₂	FM ^{a,}	>300 ^a	Metallic	T_{CDW} ~ 130 K MBE-grown	MSe ₂ 
MnSe _x	FM ^{a,⊥}	>300 ^a	3.4	MBE-grown	CrX ₃ 
CrI ₃	L-AFM ^{a,⊥} FM ^{b,⊥}	45 ^a –61 ^b	1.2		
CrBr ₃	FM [⊥]	20 ^a –37 ^b	2.2		
CrCl ₃	L-AFM	17	3.0		

^aAtomically thin. ^bUnexfoliated bulk. ^{||}In-plane anisotropy. [⊥]Out-of-plane anisotropy. FM, ferromagnet; AFM, antiferromagnet; L-AFM, layered antiferromagnet.

mode at 151 cm⁻¹ and disappearance of the 155 cm⁻¹ mode occurs below T_N (refs. 42,43). Whether magnetic order persists down to a single layer in these two materials is speculative. Although the splitting of P_2 in monolayer NiPS₃ is absent, a broad two-magnon feature is still present, interpreted to indicate the presence of short-range magnetic order⁴¹. In monolayer MnPS₃, the 151 cm⁻¹ and 155 cm⁻¹ modes were not detected^{42,43}, suggesting the suppression of magnetic order. These examples highlight limitations of Raman spectroscopy in probing antiferromagnetism down to the monolayer limit and the necessity for developing experimental techniques (see Box 1) that can directly probe antiferromagnetic order in atomically thin magnetic vdW materials.

CrGeTe₃, Chromium germanium telluride (CrGeTe₃) is a semiconductor isostructural to the XPS₃ system (Table 1) and orders as a Heisenberg ferromagnet with weak out-of-plane anisotropy below its Curie temperature (T_C) of 68 K (ref. 61). Raman measurements on exfoliated thin flakes found the presence of spin–phonon coupling and the suppression of magnetic quasi-elastic scattering when cooled below T_C (ref. 62). Electrical transport measurements on a five-layer flake of CrGeTe₃ encapsulated between two hexagonal boron nitride (hBN) layers show ambipolar field-effect transistor behavior down to 40 K with the application of a gate voltage⁶³, demonstrating the ability to access free carriers in both the conduction and valence bands. Furthermore, magneto-optical Kerr effect (MOKE; see Box 1) measurements at 40 K reveal magnetic hysteresis for the hBN-encapsulated five-layer flake, demonstrating its long-range ferromagnetic order. For atomically thin unencapsulated flakes, there is a strong magnetic field-dependent critical temperature between ferromagnetic-like behaviour and paramagnetism, shown in Fig. 1c¹⁴. In 2D magnetic systems with low anisotropy like CrGeTe₃ (<1 μeV), although intrinsic long-range magnetic order may be suppressed by thermal fluctuations, a strong magnetic

susceptibility remains. This provides responsive control over the magnetic state of such materials with external fields¹⁴.

Fe₃GeTe₂, Iron germanium telluride (Fe₃GeTe₂) is an itinerant ferromagnet with strong out-of-plane anisotropy in the bulk that has T_C of ~220 K (refs. 64–68). This compound contains three-atom-thick slabs of composition Fe₃Ge with Fe–Fe and Fe–Ge bonding between layers of Te anions (Table 1). A similar vdW material, Fe₂GeTe₂, has a more complex and thicker slab of iron and germanium between the Te layers, and T_C above room temperature at around 310 K (ref. 54). These two materials are difficult to mechanically exfoliate, requiring a gold^{69–71} or alumina-assisted (Al₂O₃) exfoliation technique⁷² to successfully isolate atomically thin flakes. Both the Curie temperature and the magnetic anisotropy of Fe₃GeTe₂ decrease as Fe vacancies are created⁶⁸.

The T_C of Fe₃GeTe₂ has a strong dependence on layer number, illustrated in Fig. 1d, accompanying a transition from 3D to 2D Ising ferromagnetism⁷³. From reflectance magneto-circular dichroism (RMCD) microscopy measurements, T_C of Fe₃GeTe₂ monolayers exfoliated onto gold and Al₂O₃ were measured to be 130 K and 70 K, respectively. Differences in the ordering temperatures between the gold- and Al₂O₃-exfoliated Fe₃GeTe₂ monolayers could be due to iron vacancies in the starting bulk crystal⁶⁸; the Al₂O₃-exfoliated Fe_{3-x}GeTe₂ crystals used in the anomalous Hall measurements (Box 1) have T_C of ~205 K and are consistent with a composition of Fe_{2.87}GeTe₂ (refs. 68,72).

Wafer-scale thin films of Fe₃GeTe₂ grown on GaAs (111) through molecular beam epitaxy (MBE) with thicknesses down to ~7 nm also display ferromagnetism with a Curie temperature around 216 K (ref. 74). Exhibiting T_C nearly identical to exfoliated samples of similar thickness, these wafer-scale Fe₃GeTe₂ films are encouraging for incorporating high-quality magnetic films in practical vdW heterostructures and devices. Room-temperature ferromagnetism

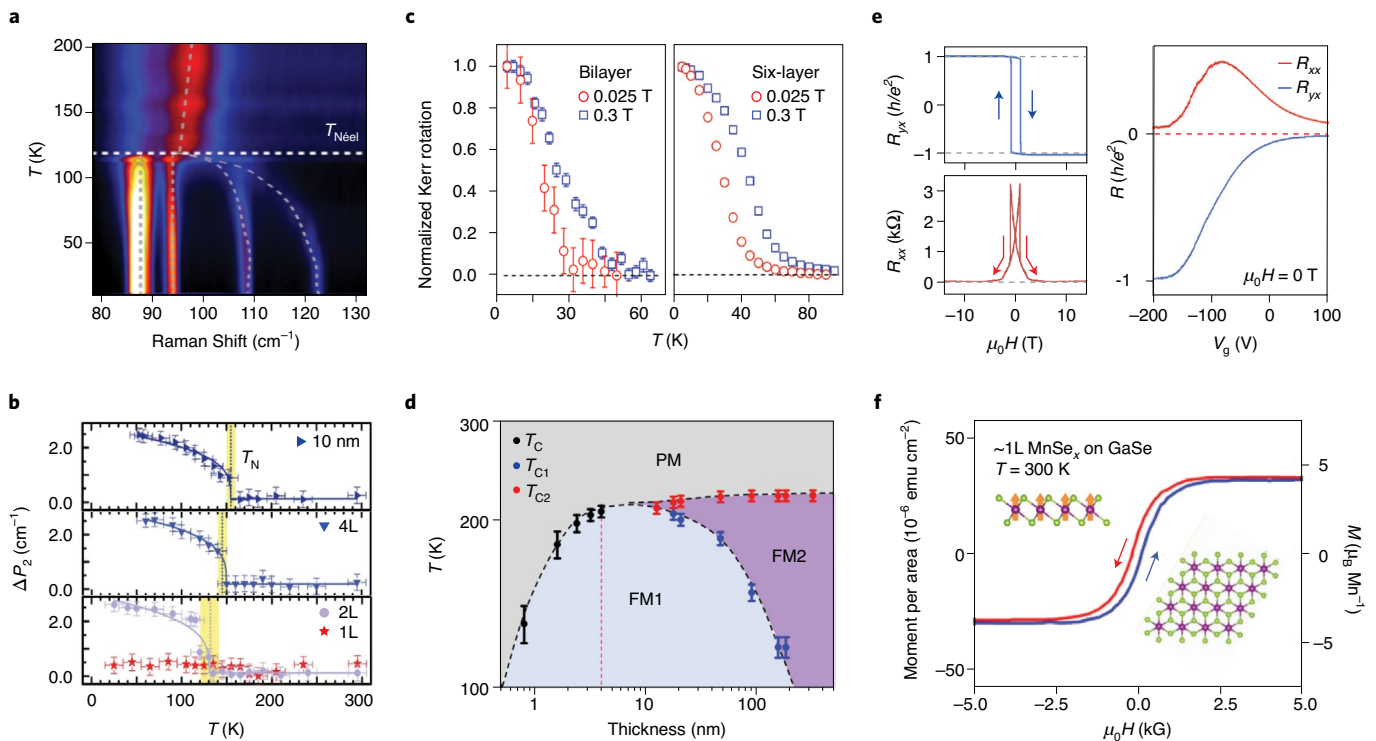


Fig. 1 | Magnetic properties of atomically thin chalcogen-based magnets. **a**, False-colour plot of temperature-dependent Raman spectra from 10 K up to 200 K taken on bulk FePS_3 . Thick white dashed line demarcates T_N at ~ 120 K. Thin grey dashed lines are guides to the eye. **b**, Temperature-dependent splitting, ΔP_2 , of the 180 cm^{-1} E_g mode in atomically thin flakes of NiPS_3 . Note the absence of splitting in the monolayer. The highlighted region denotes the inferred T_N . Error bars denote experimental uncertainties. Solid lines are fitting results from a spin-induced phonon frequency shift model⁴¹. **c**, Temperature-dependent Kerr rotation signal of a bilayer and a six-layer CrGeTe_3 flake in a constant applied magnetic field of 0.025 T (red) and 0.3 T (blue). Dashed line indicates zero Kerr signal. Error bars indicate one standard deviation. **d**, Temperature–thickness phase diagram of Fe_3GeTe_2 exfoliated on gold. The black dots show measurements of T_C on mono- to five-layer flakes, the blue dots are the measured transition temperatures, T_{C1} , between single-domain ferromagnetism (FM1; blue) and labyrinthine-domain ferromagnetism (FM2; purple), while the red dots indicate the transition temperature, T_{C2} , between labyrinthine-domain ferromagnetism and the paramagnetic phase (PM; grey). Red dashed line indicates the critical thickness at which the dimensional crossover between 2D and 3D Ising behaviour occurs. Black dotted lines are guides to the eye. Error bars indicate one standard deviation. **e**, Left two panels show magnetic field-dependent transport measurements of R_{xx} (red) and R_{yx} (blue) on a five septuple layer (SL) MnBi_2Te_4 flake with an applied gate voltage of -200 V at 1.4 K. Quantized Hall signal of -0.97 h/e^2 is observed in the R_{yx} channel at zero applied magnetic field. R_{xx} is nearly zero when out-of-plane magnetic fields exceed 2 T in magnitude. Black dashed lines in R_{yx} demarcates $\pm h/e^2$ and in R_{xx} marks zero resistance. Arrows indicate magnetic field sweep direction. Right panel shows gate voltage-dependent R_{xx} and R_{yx} measurements of the same device at 1.6 K at zero applied magnetic field. Quantized behaviour is observed as the gate voltage approaches -200 V. Red dashed line demarcates zero resistance. **f**, Magnetic-field dependent SQUID measurements of the magnetization at 300 K of $\sim 1\text{L MnSe}_x$ grown on GaSe substrate through MBE. The insets show a side view (upper-left) and top view (lower-right) of monolayer MnSe_x . Orange arrows illustrate the spin direction in the ferromagnetic state. Blue and red arrows depict the magnetic field sweep direction. Figure adapted with permission from: ref. ⁵⁰, American Chemical Society (**a**); ref. ⁴¹, Springer Nature Ltd (**b**); ref. ¹⁴, Springer Nature Ltd (**c**); ref. ⁷³, Springer Nature Ltd (**d**); ref. ⁵⁹, AAAS (**e**); and ref. ⁵³, American Chemical Society (**f**).

has also been observed in trilayer $\text{Fe}_{3-x}\text{GeTe}_2$ flakes upon ionic liquid gating⁷². One possible origin of this room-temperature magnetism could be the creation of magnetic Fe_{2-x}Ge defects through intercalant-induced degradation of the $\text{Fe}_{3-x}\text{GeTe}_2$ layers⁷⁵. Although such degradation has been observed in bulk, there has been no structural characterization to confirm the presence of Fe_{2-x}Ge defects in atomically thin $\text{Fe}_{3-x}\text{GeTe}_2$ flakes. Monolayers of Fe_3GeTe_2 have not yet been isolated, though flakes about 12 nm thick (about three unit cells or 12 layers) exfoliated onto SiO_2/Si substrates were shown to display ferromagnetic order with T_C near 270 K (ref. ⁵⁴). These recent advancements are promising for realizing room-temperature magnetism in exfoliated 2D magnets down to the monolayer limit.

MnBi_2Te_4 . Manganese bismuth telluride (MnBi_2Te_4) is the first topological insulator to display intrinsic magnetic order³⁸. The compound contains seven-atom-thick layers with a triangular net of Mn^{2+} bonded to two $[\text{BiTe}_2]^{1-}$ layers (Table 1). Below 25 K,

A-type (layered) antiferromagnetism is observed in the bulk^{38,55} where spins within each layer order ferromagnetically and adjacent layers arrange antiferromagnetically. Upon the application of an out-of-plane magnetic field of about 3.5 T, MnBi_2Te_4 bulk crystals undergo a spin-flop transition from the layered antiferromagnetic ground state to a canted antiferromagnetic state where all spins mostly point out-of-plane with in-plane components pointing oppositely between layers⁵⁵. Topological insulator behaviour was shown through density functional theory (DFT) calculations³⁸ and angle-resolved photoemission spectroscopy (ARPES) measurements³⁸ where the presence of Dirac-like surface states at the Γ point demonstrate non-trivial topology in MnBi_2Te_4 . The magnetic anisotropy and interlayer exchange coupling strength changes upon Sb substitution⁵⁶.

Similar materials, $\text{MnBi}_{2n}\text{Te}_{3n+1}$ ($n = 2-6$), which can be visualized as charge-balanced alternating layers of MnBi_2Te_4 and Bi_2Te_3 , have also been synthesized⁵⁷. MnBi_4Te_7 and $\text{MnBi}_6\text{Te}_{10}$ both exhibit

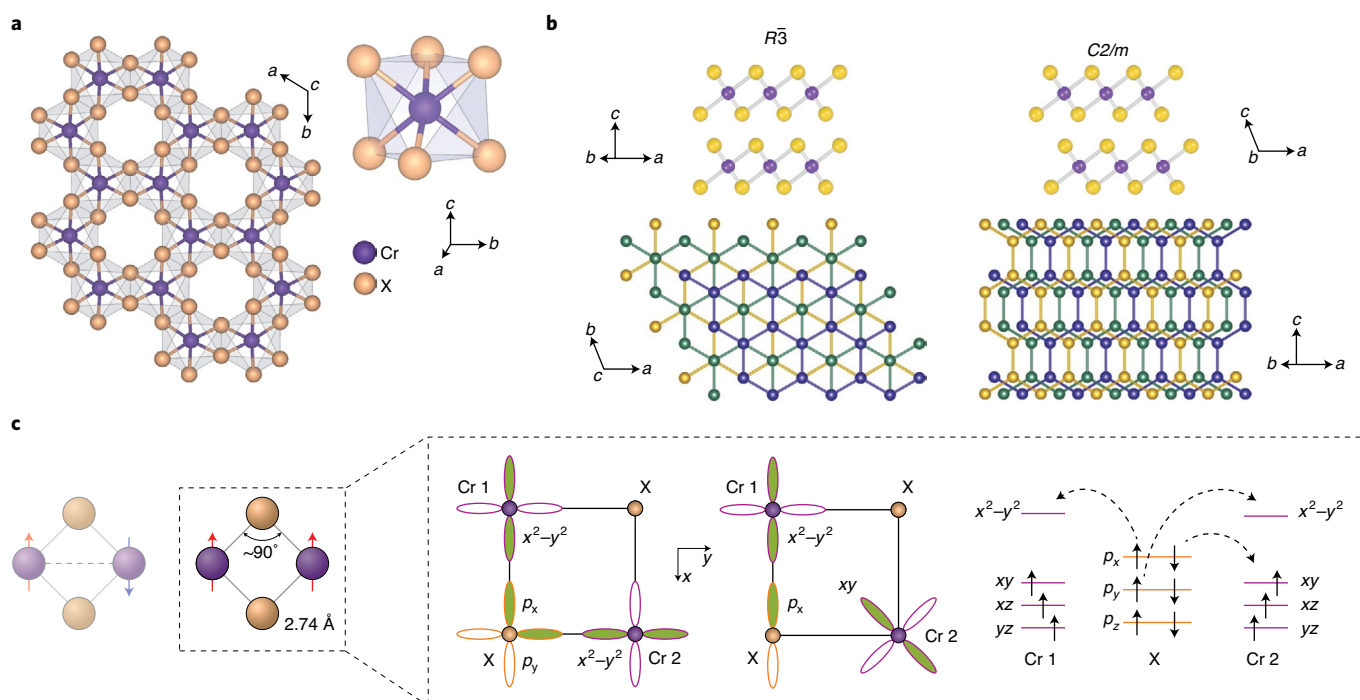


Fig. 2 | Structural and magnetic properties of layered chromium trihalides. **a**, Top view of a CrX_3 monolayer along with an illustration of the coordination between Cr^{3+} (purple) and X^- (gold) in an octahedral cage. **b**, Side (upper-half) and top views (lower-half) of the CrX_3 layers in the rhombohedral (left) and monoclinic (right) phases. Three CrX_3 layers are shown without the Γ ions to show the relative stacking order of the bottom (yellow), middle (green) and top (blue) Cr^{3+} layers in both phases. **c**, Illustrations of direct exchange (left, unboxed) and superexchange pathways (right, boxed) in CrX_3 . Virtual hopping of electrons between the X^- anion and Cr^{3+} occurs through two paths. The first path bridges an X^- p_x and p_y orbital with the x^2-y^2 orbitals of both Cr^{3+} ions. The second path links the X^- p_x orbital to the x^2-y^2 orbital of one Cr^{3+} ion and the xy orbital of the second Cr^{3+} ion. Both paths lead to ferromagnetism between adjacent Cr^{3+} sites. Figure adapted with permission from: ref. ¹¹¹, Springer Nature Ltd (**a**); ref. ³¹, Springer Nature Ltd (**b**); and ref. ⁹⁶, IOP (**c**).

A-type antiferromagnetism below 13 and 11 K, respectively, and possess a lower critical field (~ 0.1 T) at which the spin-flop transition occurs. From ARPES, MnBi_4Te_7 and $\text{MnBi}_6\text{Te}_{10}$ are intrinsic magnetic topological insulators, making these intrinsic vdW heterostructures of atomically thin magnetic layers spaced by atomically thin topological layers. No work has been done yet to study the exfoliated flakes of these crystals.

DFT calculations further predict that thin MnBi_2Te_4 samples with an odd number of layers are quantum anomalous Hall (QAH) insulators, while MnBi_2Te_4 samples with even number of layers are axion insulators⁵⁸. Promising experimental progress has been made toward this type of state. Quantized Hall conductance is seen in exfoliated thin flakes (Fig. 1e)^{39,59,60}, while in an exfoliated six-layer MnBi_2Te_4 flake, zero ρ_{xy} with large ρ_{xx} is observed, where ρ_{xx} is the longitudinal resistivity and ρ_{xy} is the Hall resistivity, when the Fermi level is tuned to within the bulk gap in a range of small magnetic fields³⁹. The latter is a signature of the axion insulator state. An applied magnetic field then enables a quantum phase transition between the axion and Chern insulator states. Nine-layer MnBi_2Te_4 devices were also discovered to exhibit a Chern number of 2 in their Chern insulator phase⁶⁰, enabling the study of high Chern number insulators. Thus, the $\text{MnBi}_{2n}\text{Te}_{3n+1}$ family is a promising new class of vdW materials with the synergistic combination of magnetism and topology.

VSe₂ and MnSe_x. In the bulk, vanadium selenide (VSe_2) is paramagnetic^{76,77} while different stoichiometries of manganese selenide (MnSe and MnSe_2) are antiferromagnetic^{78,79}. Single layers of the compounds contain triangular nets of tetravalent Mn or V separated by close-packed planes of Se^{2-} anions (Table 1). When monolayer films of these materials are grown by MBE on vdW substrates

(highly ordered pyrolytic graphite (HOPG) or molybdenum sulfide (MoS_2) for VSe_2 (refs. ^{52,80}), and gallium selenide (GaSe_2) or tin selenide (SnSe_2) for MnSe_x (ref. ⁵³)), ferromagnetic order survives up to room temperature, as observed by vibrating sample and superconducting quantum interference device (SQUID) magnetometry (Fig. 1f). A question that remains to be answered is whether this ferromagnetism is intrinsic to these MBE-grown monolayers or is a result of other mechanisms such as interfacial effects or defects⁸⁰. Although DFT studies predict ferromagnetic ground states in VSe_2 and MnSe_x monolayers^{81,82}, they do not account for competing phases such as charge density wave formation in VSe_2 (refs. ^{83,84}), or the role of anisotropy in determining the magnetic ground state⁸⁵. This matter is supported by conflicting experimental studies on MBE-grown VSe_2 monolayers that show a lack of intrinsic ferromagnetism through SQUID magnetometry^{83,86}, scanning tunnelling microscopy (STM)^{84,86}, ARPES^{84,86,87} and helicity-resolved X-ray absorption at the V $L_{2,3}$ edge^{83,86,87}, which hints at a frustrated magnetic ground state⁸⁶. These cases point to the challenge of understanding vdW materials that are grown and not exfoliated: structural characterization of the as-grown systems can be challenging, yet minor structural distortions or the presence of defects can be important aspects of any magnetic system like in metallic ultrathin films¹⁸ and metal-oxide perovskite heterostructures¹⁹.

Chromium trihalides in the atomically thin limit

The halogen-based magnetic vdW materials that have been exfoliated to the ultrathin regime consist of the chromium trihalides (CrX_3 , $\text{X} = \text{Cl}, \text{Br}, \text{I}$), the ferromagnet vanadium triiodide (VI_3)^{88–90} and the quantum spin liquid candidate ruthenium trichloride ($\alpha\text{-RuCl}_3$). Of the materials listed, only the CrX_3 family has been extensively studied in the atomically thin limit, which has been a

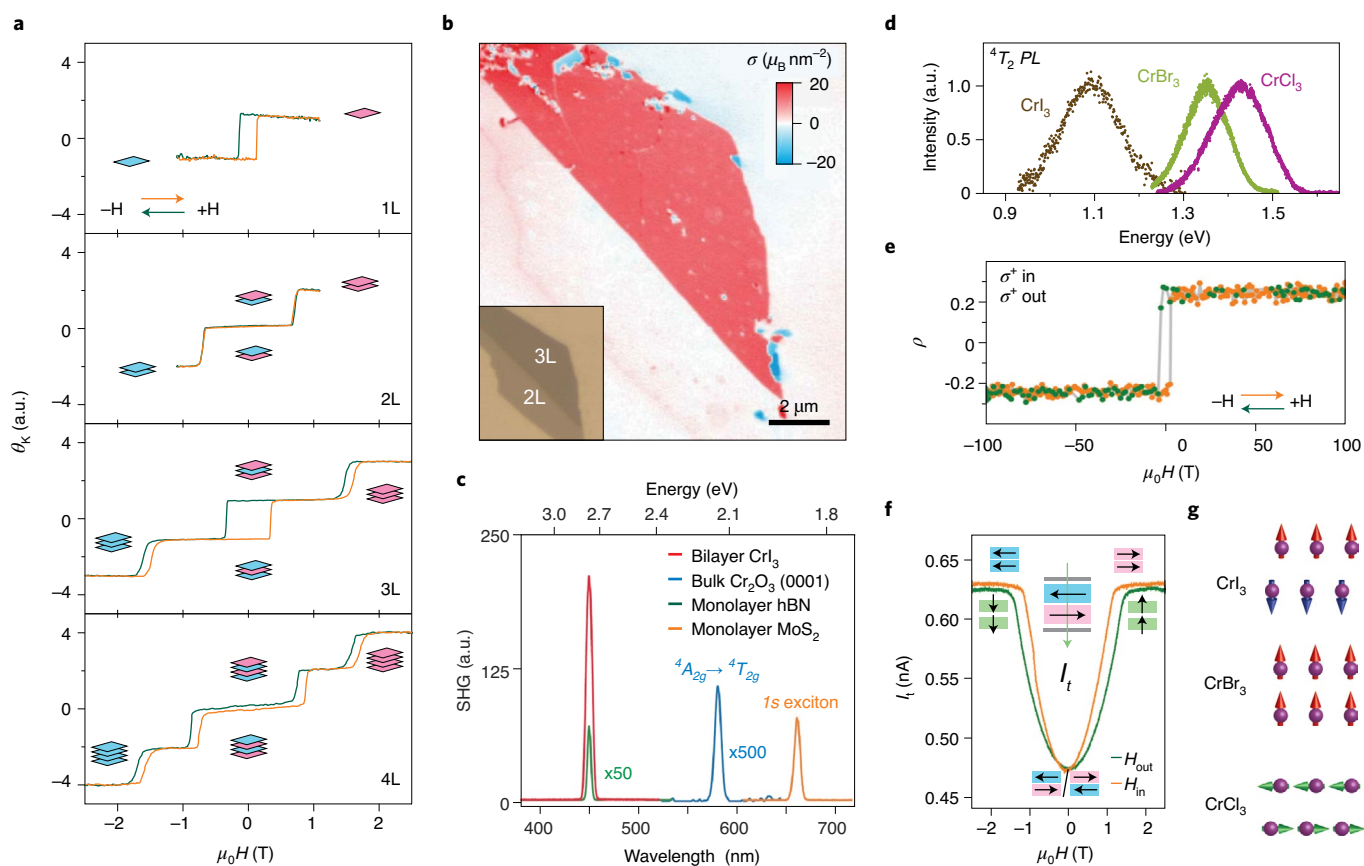


Fig. 3 | Magnetic properties of atomically thin chromium trihalides. **a**, Kerr signal, θ_K , of mono- to four-layer CrI_3 as a function of magnetic field. The green (orange) curve shows MOKE data taken as the magnetic field is swept down (up). The MOKE measurements for the monolayer and bilayer samples were taken at 15 K. The trilayer and four-layer Kerr signals were measured at 2 K. Cartoons illustrate the magnetic ground states and fully spin-polarized states. **b**, Magnetization map of a bi- and trilayer CrI_3 flake at 7 K in a magnetic field of 175 mT. The dark red area, depicting a net magnetization pointing out of the page, is the trilayer portion of the CrI_3 flake. The maps are reduced from stray field maps taken by scanning diamond nitrogen-vacancy centre magnetometry. The inset is an optical micrograph of the bi- and trilayer flake shown in the magnetization map. **c**, SHG signal of a bilayer CrI_3 flake (red), a monolayer hBN flake (green), bulk Cr_2O_3 (0001) (blue), and a monolayer MoS_2 flake (yellow). The SHG signal from bulk Cr_2O_3 and monolayer MoS_2 is resonant with the ${}^4A_{2g} \rightarrow {}^4T_{2g}$ transition and 1s exciton, respectively. All signals are normalized to the same laser power of 0.6 mW. **d**, Normalized photoluminescence from the 4T_2 transition in monolayers of CrI_3 (olive), CrBr_3 (green) and CrCl_3 (magenta). Measurements were taken at 15 K for monolayer CrI_3 (ref. ¹¹¹), 5 K, for monolayer CrBr_3 (ref. ¹¹²), and 2 K for monolayer CrCl_3 (ref. ²⁹). **e**, Normalized intensity difference, ρ , between right-circularly polarized and left-circularly polarized 4T_2 photoluminescence as a function of magnetic field in a bilayer CrBr_3 flake. The green (orange) curve shows photoluminescence data taken as the magnetic field is swept down (up). **f**, Magnetic field-dependent tunnelling measurements of a bilayer CrCl_3 flake at 2 K using an in-plane field (orange) and an out-of-plane field (green). Cartoons depict the magnetic ground states and spin-polarized states for the CrCl_3 bilayer. **g**, Illustrations showing the magnetic ground states of bilayer CrI_3 (top), CrBr_3 (middle) and CrCl_3 (bottom). Figure adapted with permission from: ref. ¹³, Springer Nature Ltd (**a**); ref. ¹⁰⁶, AAAS (**a**); ref. ¹⁰⁹, AAAS (**b**); ref. ¹¹⁰, Springer Nature Ltd (**c**); ref. ¹¹¹, Springer Nature Ltd (**d**); ref. ¹¹², American Chemical Society (**d,e**); and ref. ²⁹, American Chemical Society (**d,f**).

model system in understanding how dimensionality and exfoliation itself modify the magnetic ground state. As such, we will solely focus on reviewing the magnetic properties of the chromium trihalides in this section, starting with a brief overview of their bulk crystal structure and magnetic properties, and then discussing work done in the atomically thin limit for each of the chromium trihalides. Those who are interested in quantum spin liquid behaviour are encouraged to consult reviews on this topic^{22,91}.

Crystal structure and magnetic properties of the bulk chromium trihalides. The chromium trihalides are a family of magnetic insulators that exhibit multiple magnetic phases and display a wide variety of magneto-optical phenomena. Within each layer, the chromium trihalides are isostructural and consist of a honeycomb network of edge-sharing octahedra formed by a central chromium coordinated to six monovalent halide anions at the corners, illustrated in Table 1

and Fig. 2a^{92,93}. As shown in Fig. 2b, these layers stack in either the ‘high-temperature’ monoclinic phase above 220 K in CrI_3 (ref. ⁹³), 420 K in CrBr_3 (ref. ⁹⁴), and 240 K in CrCl_3 (refs. ^{31,94,95}), or the ‘low-temperature’ rhombohedral phase. Hence, bulk CrBr_3 crystals are in the low-temperature rhombohedral crystallographic phase even at room temperature.

Superexchange coupling mediated through the halide ions serves as the predominant exchange pathway in the chromium trihalides (Fig. 2c). The $\sim 90^\circ$ bond angle formed by two adjacent Cr^{3+} sites and a halide ion leads to ferromagnetic order within a single layer as intuited by the Goodenough–Kanamori–Anderson rules^{92,96,97}. In the bulk, adjacent layers show ferromagnetic interlayer exchange in CrI_3 and CrBr_3 (refs. ^{93,98,99}), and antiferromagnetic interlayer exchange in CrCl_3 (refs. ^{95,100–102}). The corresponding magnetic ordering temperatures are 61 K (ref. ⁹³) for CrI_3 , 37 K for CrBr_3 (ref. ⁹⁹), and 17 K for CrCl_3 (ref. ⁹⁵). The magnetic anisotropies also

differ, with CrI_3 and CrBr_3 both exhibiting an out-of-plane easy axis^{93,98} and CrCl_3 displaying easy-plane anisotropy^{95,100–102}. This was theoretically found to be the result of spin–orbit coupling induced by the halide anion in the Cr–X–Cr superexchange pathway⁸⁵. Larger spin–orbit coupling leads to increased out-of-plane anisotropy, verified through estimates of the anisotropy strength from electron paramagnetic resonance measurements¹⁰³. The strength and direction of the magnetic anisotropy is also shown to be controllable through halide substitution in solid solutions of $\text{CrCl}_{3-x}\text{Br}_x$ (ref. 104).

CrI₃. Exfoliated monolayers retain long-range ferromagnetic order, clearly seen through magnetic hysteresis in MOKE microscopy measurements when cooled below their Curie temperature of 45 K (ref. 13). This slight decrease of the monolayer T_C from the bulk value of 61 K is a consequence of the strong anisotropy that persists down to the single-layer limit⁸⁵. The Kerr signal measured from a monolayer of CrI_3 can also be enhanced by thin film interference with the underlying SiO_2/Si substrate, with rotations of 5 mrad observed in reflected linearly polarized 633 nm light^{13,105}.

On the other hand, few layers (≥ 2) of CrI_3 exhibit antiferromagnetic stacking of the layers in their ground state, that is, A-type antiferromagnetism^{13,23–25,106}. This is in stark contrast to the ferromagnetic order observed in bulk and results from the dependence of interlayer exchange on the layer stacking sequence are discussed in more detail in the section ‘Tunable stacking-order-dependent magnetism’. In bilayer CrI_3 , applying an out-of-plane magnetic field of ~ 0.7 T induces a spin-flip transition from the layered antiferromagnetic state to a ferromagnetic-like state where all spins point along the field direction. For thicker flakes of CrI_3 , layer-by-layer switching occurs as the magnetic field is increased, resulting in intermediate magnetic states that have also been observed in both metallic^{18,107} and all-oxide¹⁰⁸ synthetic magnetic multilayer films. The magnetic hysteresis and spin-flip behaviour for mono- to four-layer CrI_3 are summarized in Fig. 3a. Additionally, diamond nitrogen–vacancy magnetometry (Box 1) determined¹⁰⁹ the magnetization of monolayer CrI_3 to be about $16.1 \mu_B \text{ nm}^{-2}$, close to the predicted value⁹³ of $14.7 \mu_B \text{ nm}^{-2}$ for a single layer of fully polarized Cr^{3+} spins. In contrast, bilayer CrI_3 was shown to exhibit no net out-of-plane magnetization, as shown in Fig. 3b. The lack of a net out-of-plane moment confirms the antiferromagnetic interlayer coupling in atomically thin CrI_3 that is observed through MOKE.

Next, we will discuss magneto-optical effects that arise in atomically thin CrI_3 . In both the monolayer and bulk, the crystal structure of CrI_3 is centrosymmetric. Inversion symmetry must be present in the bilayer as translations of the top layer relative to the bottom layer preserves centrosymmetry. Consequently, processes that only occur in the absence of inversion symmetry, such as second harmonic generation (SHG), are forbidden. Despite these symmetry arguments, strong SHG is observed when the bilayer is in a layered antiferromagnetic state¹¹⁰. Highlighted in Fig. 3c, its second-order susceptibility $|\chi^{(2)}|$ is several orders of magnitude larger than $|\chi^{(2)}|$ of model systems of magnetism-induced SHG (for example, Cr_2O_3), several times larger than $|\chi^{(2)}|$ of monolayer hBN, and comparable to $|\chi^{(2)}|$ of monolayer transition metal dichalcogenides. Only when the bilayer is switched to the fully spin-polarized state, or warmed above its T_N , is the SHG signal suppressed. Thus, it is the layered antiferromagnetic order that breaks inversion symmetry in bilayer CrI_3 that leads to the non-reciprocal SHG. It remains unclear from a microscopic understanding why the SHG is so large.

Spontaneous helical light emission at 1.1 eV (Fig. 3d) has also been observed from both the monolayer and bilayer through photoluminescence measurements¹¹¹. The degree of circular polarization, defined as the normalized intensity difference between the two helicities of emitted light, was found to be $\sim 50\%$ in both the

ferromagnetic monolayer and the fully spin-polarized bilayer, and $\sim 0\%$ in antiferromagnetic bilayers. The helicity of the emitted light also tracked the net magnetization, with σ^+ (σ^-)-polarized light emitted when the net magnetization pointed up (down). This helical light emission originates from the Stokes-shifted recombination of d - d excitons localized at the Cr sites and depends sensitively on sources of local symmetry breaking such as from trigonal distortion, odd-parity phonons, and interactions with excited states and spin–orbit coupling^{105,111}. Furthermore, the intensity of emitted light per layer increases for thicker flakes, indicating that processes that relax the d - d selection rule are affected by substrate or interlayer interactions. As a result, these d - d selection rules could potentially be tuned by external knobs such as strain or pressure, allowing control over the spontaneous helical light emission from a 2D magnetic insulator.

CrBr₃. Just like monolayers of CrI_3 , monolayers of CrBr_3 display ferromagnetism (Fig. 3e). Spontaneous emission of helical light can also be seen at 1.35 eV from CrBr_3 down to the monolayer limit (Fig. 3d), albeit with a lower degree of circular polarization ($\sim 20\%$)¹¹² than CrI_3 monolayers and fully spin-polarized bilayers. The origin of this photoluminescence is believed to be the same as for the spontaneous light emission in CrI_3 , that is, from a weakly allowed d - d molecular orbital transition. T_C of monolayer CrBr_3 only decreases slightly from the bulk, independently determined to be 30 K from RMCD³⁰, helicity-resolved photoluminescence¹¹², and graphene Hall bar micro-magnetometry measurements³³.

Distinct from CrI_3 , ferromagnetic order is prevalent for all thicknesses of CrBr_3 flakes (see discussion of layer stacking and magnetic order in the section ‘Tunable stacking-order-dependent magnetism’). Samples thicker than ~ 8 nm deviate from the simple magnetic hysteresis behaviour of single-domain uniaxial ferromagnets, instead displaying magnetic behaviour resembling the formation of nanoscale labyrinthine domains smaller than the laser spot. Although these nanoscale domains were not directly observed in CrBr_3 , they have been imaged through magnetic force microscopy (MFM; see Box 1) on bulk Fe_3GeTe_2 (ref. 73). This behaviour is typical for thin-film ferromagnets, where the balance of magnetic anisotropy, saturation magnetization and aspect ratio (thickness versus lateral dimensions) determines the critical thickness at which domain formation switches between the two different length scales¹¹³.

CrCl₃. CrCl_3 has been shown to be exfoliable down to the monolayer limit⁹⁵, though no experimental work to investigate its magnetic properties has been reported so far. Recent work on CrCl_3 has instead focused on studying ultrathin flakes through tunnelling transport measurements^{29–31}. Layered antiferromagnetism persists down to the bilayer with a thickness-independent T_N of ~ 14 K (refs. 29–31). The application of an in-plane magnetic field induces a spin-flop transition to a canted antiferromagnet state before rotating to a fully spin-polarized state that is aligned with the magnetic field. For out-of-plane magnetic fields, only spin canting is observed. Bilayer flakes reach an out-of-plane fully spin-polarized state at magnetic fields over 1.3 T, as can be seen in Fig. 3f^{29–31}, larger than the 0.7–1 T fields needed for in-plane magnetic saturation. The tunnelling resistance is independent of the in-plane magnetic field direction²⁹. All these measurements imply that individual CrCl_3 layers are easy-plane ferromagnets, with shape anisotropy being the dominant form of magnetic anisotropy³¹, consistent with the magnetic order observed in bulk⁹⁵. The magnetic order of monolayer CrCl_3 then is expected to be closely approximated by the 2D XY model^{29,95,100–102}. This could enable the study of topological vortices and the Berezinskii–Kosterlitz–Thouless transition in a 2D magnetic insulator. The magnetic order of atomically thin CrX_3 is summarized pictorially in Fig. 3g.

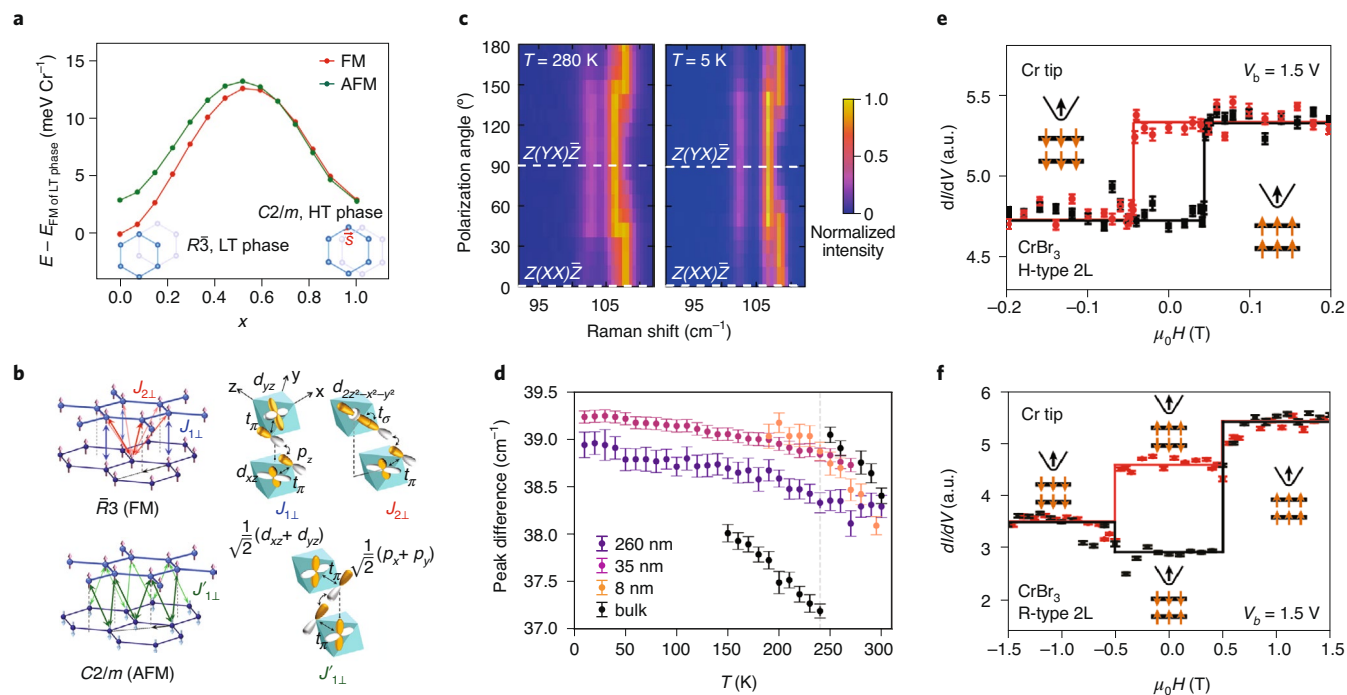


Fig. 4 | Stacking order and super-superexchange interactions in CrX_3 . **a**, Energy plot of the ferromagnetic (red) and layered antiferromagnetic states (green) for bilayer CrI_3 as a function of sliding distance, x , along the direction, \mathbf{s} , that is depicted in the lower-right cartoon. Rhombohedral and monoclinic stacking occur when $x = 0$ and when $x = 1$, respectively, and are illustrated in cartoons on the lower-left and lower-right. Ferromagnetism is preferred in the rhombohedral phase while layered antiferromagnetism is weakly preferred in the monoclinic phase. **b**, Interlayer super-superexchange (SSE) pathways between Cr^{3+} of adjacent layers. The top half illustrates SSE pathways for rhombohedral-stacked bilayers while the bottom half depicts the SSE pathway for monoclinic-stacked bilayers. Summing all interlayer SSE pathways results in ferromagnetic order in rhombohedral-stacked bilayers and layered antiferromagnetic order in monoclinic-stacked bilayers. **c**, Colour map of the polarization-dependent Raman spectra in a 4-nm-thick CrI_3 flake near room temperature at 280 K (left) and at 5 K (right). The white dashed lines in the bottom and centre represent co-linear and cross-linear detection, respectively. **d**, Temperature-dependent peak energy of the 247 cm^{-1} peak plotted as the energy difference between the 247 cm^{-1} and 209 cm^{-1} peaks in bulk single-crystal CrCl_3 (black) and an exfoliated 260-nm- (purple), 35-nm- (pink) and 8-nm-thick (orange) CrCl_3 flake. The grey dashed line denotes the structural transition temperature of bulk CrCl_3 . Error bars denote one standard deviation of determining the Raman peak positions. **e**, Magnetic field-dependent spin-polarized tunnelling conductance through H-type stacked bilayer CrBr_3 . Hysteresis is clearly seen, implying ferromagnetism in bilayer CrBr_3 films. A bias of 1.5 V was applied between the Cr tip and the underlying HOPG substrate. Cartoons depict the relative magnetization alignments of the Cr tip and the CrBr_3 bilayer film. The Cr tip was pinned in the spin-up configuration for the entire field range. **f**, Same as **e** but for R-type stacked bilayer CrBr_3 . Layered antiferromagnetic order can clearly be seen for R-type stacked CrBr_3 films. These results underscore the importance of stacking order in determining the magnetic ground state in atomically thin CrBr_3 . Error bars for **e** and **f** represent one standard deviation. Solid lines are guides to the eye. Figure adapted with permission from: ref. ¹¹⁴, APS (**a**); ref. ¹¹⁷, American Chemical Society (**b**); ref. ¹¹⁶, IOP (**c**); ref. ³¹, Springer Nature Ltd (**d**); and ref. ¹¹⁹, AAAS (**e, f**).

Tunable stacking-order-dependent magnetism

Due to the large vdW gap between adjacent layers, interlayer exchange interactions between localized spin sites are dominated by super-superexchange interactions mediated by virtual electron hopping through two anions, rather than conventional direct exchange and one-anion superexchange interactions^{28,114}. Since these superexchange pathways are highly sensitive to changes in both the interatomic distances and, more importantly, the bond angles^{97,115}, identifying the stacking order of layered vdW magnets is imperative in determining their magnetic ground state. In bulk CrX_3 , for example, the individual layers stack in the monoclinic phase at high temperatures and undergo a structural transition to stack in the rhombohedral phase at low temperatures, as confirmed by X ray diffraction measurements^{93–95}, and polarization-dependent Raman measurements^{27,31,116}. DFT calculations find the two structures to be nearly degenerate (Fig. 4a)^{114,117}. Depending on which structural phase the CrX_3 crystal is in, different combinations of X p orbitals mediate the interlayer exchange interactions, as illustrated in Fig. 4b^{114,117}. In CrI_3 , interlayer antiferromagnetic and ferromagnetic behaviour is predicted in the monoclinic and rhombohedral

phases, respectively. For CrCl_3 , layered antiferromagnetic behaviour is expected for both crystal structures, though the interlayer exchange interaction strength is much weaker in the rhombohedral phase³¹. Given that both bulk CrI_3 and CrCl_3 are in the rhombohedral phase below their magnetic ordering temperatures, it is no surprise that ferromagnetism and layered antiferromagnetism are observed, respectively^{93–95}.

For atomically thin flakes of CrI_3 and CrCl_3 , the room-temperature stacking orders are in the monoclinic phase (the same as in bulk), observed by the fourfold structure in the Raman polarization dependence of the 107 cm^{-1} (Fig. 4c, left panel) and 247 cm^{-1} peaks, respectively^{27,31,116}. Surprisingly, this fourfold pattern persists down to 5 K in CrI_3 (refs. ^{27,116}) (Fig. 4c, right panel) and 80 K in CrCl_3 (ref. ³¹). In addition to the persistence of a fourfold polarization pattern, exfoliated CrCl_3 flakes of thicknesses up to 260 nm exhibit no abrupt energy shift in the 247 cm^{-1} peak even down to 10 K, as shown in Fig. 4d³¹. In contrast, the 247 cm^{-1} peak redshifts by 2 cm^{-1} at around 240 K in unexfoliated, bulk crystals, indicating a structural transition that is absent in the exfoliated CrCl_3 flakes. Furthermore, polarization-dependent SHG measurements shows

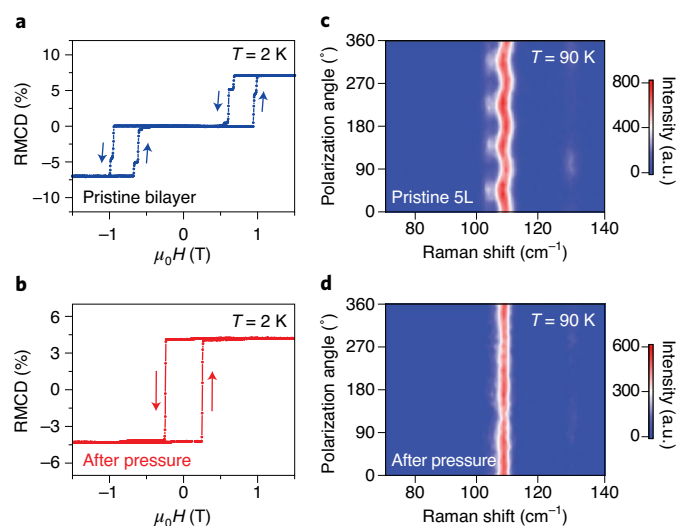


Fig. 5 | Pressure control of magnetic states in few-layer CrI₃. **a,b**, Magnetic field-dependent RMCD signal taken on a pristine bilayer (**a**) and a pressed bilayer (**b**). Arrows indicate the magnetic field sweep direction. Clearly, pressed bilayers are no longer layered antiferromagnets, but ferromagnets. **c,d**, Polarization-dependent Raman spectra of a five-layer CrI₃ flake **c**, prior to and **d**, after pressing. The disappearance of the fourfold pattern in the 107 cm⁻¹ mode after pressing indicates a structural phase transition from monoclinic to rhombohedral stacking. Figure adapted with permission from: ref. ²⁶, Springer Nature Ltd (**a,b**); and ref. ²⁷, Springer Nature Ltd (**b,c**).

twofold rotational symmetry with a mirror plane in CrI₃ bilayers, consistent with the C_{2h} symmetry of the monoclinic phase¹¹⁰. Conclusively, exfoliated CrI₃ and CrCl₃ flakes remain in the monoclinic phase even when cooled down below their respective bulk structural transition temperatures.

This monoclinic phase is responsible for the observed layered antiferromagnetic behaviour in few-layer CrI₃, consistent with theoretical calculations^{114,117}. For CrCl₃, the magnetic field required to reach magnetic saturation in atomically thin flakes is close to an order of magnitude larger than that in the bulk^{31,95,118}. This implies an enhancement of interlayer exchange by nearly an order of magnitude in atomically thin CrCl₃ and is also a result of their monoclinic crystal structure³¹.

A more direct approach to identify the interplay between the layer stacking arrangement and magnetic order is by spin-polarized STM (see Box 1) and scanning tunnelling spectroscopy (STS). Recently, bilayer films of CrBr₃ have been grown by MBE. Atomically resolved STM imaging reveals two types of stacking order: H-type and R-type. Using spin-polarized STS, ferromagnetism (Fig. 4e) and interlayer antiferromagnetism (Fig. 4f) are directly correlated to the H- and R-type stacking, respectively¹¹⁹.

In both atomically thin CrI₃ and CrCl₃, the stacking order is identical to that of the high-temperature phase observed in their bulk. The underlying mechanism for why their crystal structures match the high-temperature phase of the bulk requires further elucidation. One possibility is the application of pressure during Scotch Tape exfoliation. It has been shown that with sufficiently large pressures, an irreversible magnetic phase transition can be induced in few-layer CrI₃ from layered antiferromagnetism to ferromagnetism (Fig. 5a,b)^{26,27,109}. Polarization-dependent Raman measurements confirm the distinct layer stacking arrangement of pressed exfoliated flakes compared to pristine ones in Fig. 5c,d^{26,27}. Thus, pressure is a useful approach to both tune magnetic order and cause magnetic switching via structural transitions in ultrathin magnetic vdW materials. Moving forward, the issue of local structure and the

structural differences between the bulk and exfoliated flakes needs to be addressed.

Magnetic vdW heterostructures and devices

Cleavable magnetic materials offer flexibility as well as new opportunities for engineering magnetic heterostructures. Here, we highlight the work that has been done so far in realizing magnetic proximity effects in the 2D limit via vdW heterostructures.

Magnetic proximity control of spin and pseudospin in monolayer semiconductors. Monolayer MX₂ (M = Mo, W; X = S, Se) are direct-gap semiconductors that host robust excitons in the +K and -K valleys with circularly polarized optical selection rules¹²⁰. The degeneracy of the valley excitons can be broken by applying a magnetic field perpendicular to the sample plane¹²¹. This manifests as an energy splitting of about 0.2 meV T⁻¹ in both exciton absorption and photoluminescence emission between +K and -K valley excitons^{122,123}. In proximity to a 2D magnet, valley excitons can be controlled by the magnetic proximity effect. For instance, in heterostructures formed by monolayer WSe₂ and atomically thin CrI₃, diagrammatically shown in Fig. 6a, valley Zeeman splitting of about 3 meV at zero applied magnetic field is observed below the Curie temperature of CrI₃, equivalent to an effective magnetic field of about 13 T (ref. ³⁶). Such large induced exchange fields are promising for realizing magnetic proximity effects that modify the properties of materials adjacent to the magnetic material. Exchange field-induced Zeeman splitting is also observed in monolayer WX₂ (ref. ³²) on grown films of 3D ferromagnet EuS (Fig. 6b), though the strength of the splitting highly depends on the interface quality between the EuS film and the WX₂ monolayer. Exfoliated vdW materials on the other hand are atomically flat. Stacking another vdW material on top of these magnetic vdW substrates naturally leads to atomically sharp interfaces that allow for consistent proximity coupling across multiple heterostructures.

At the CrI₃-WSe₂ heterostructure interface, the conduction band of WSe₂ lies above the spin-polarized e_g band of CrI₃, implying spin-dependent charge hopping between WSe₂ and CrI₃ (ref. ³⁶). This leads to large spontaneously circularly polarized photoluminescence, that is, valley polarization. Due to the clean heterostructure interface, both valley Zeeman splitting and polarization have clean hysteresis curves as a function of magnetic field. The integration of magnetism through proximity effects makes WSe₂ a proximitized ferromagnetic semiconductor. Even though the net magnetization of few-layer CrI₃ evolves monotonically as a function of magnetic field, the sign of the valley Zeeman splitting and polarization can switch multiple times as layer-by-layer magnetic alignment occurs, seen in Fig. 6c^{36,37}. This implies that the valley exciton dynamics have a strong dependence on the local magnetization of layers at the heterostructure interface. Additionally, with just a small change in the laser excitation power, an extensive tuning of the valley polarization and valley Zeeman splitting can be realized in monolayer WSe₂/CrI₃ heterostructures (Fig. 6d,e). The exact origins of this power-dependent tunability is not known with one suggested possibility being laser-induced heating of the lattice³⁷. Such tunability though provides a new approach to control the valley properties of monolayer WSe₂ without having to sweep a magnetic field over the equivalent range of 20 T (ref. ³⁷).

Proximitized anomalous Hall effect, spin-orbit torque switching, and micromagnetometry. Probing the magnetism through lateral transport in ultrathin vdW magnetic semiconductors and insulators is challenging since they become too electrically insulating at temperatures below T_c (refs. ^{23–25,63}). One solution is to induce magnetic polarization in an adjacent non-magnetic metallic layer through interfacial coupling with the magnetically ordered vdW material. This has been done previously using a wide variety of non-magnetic

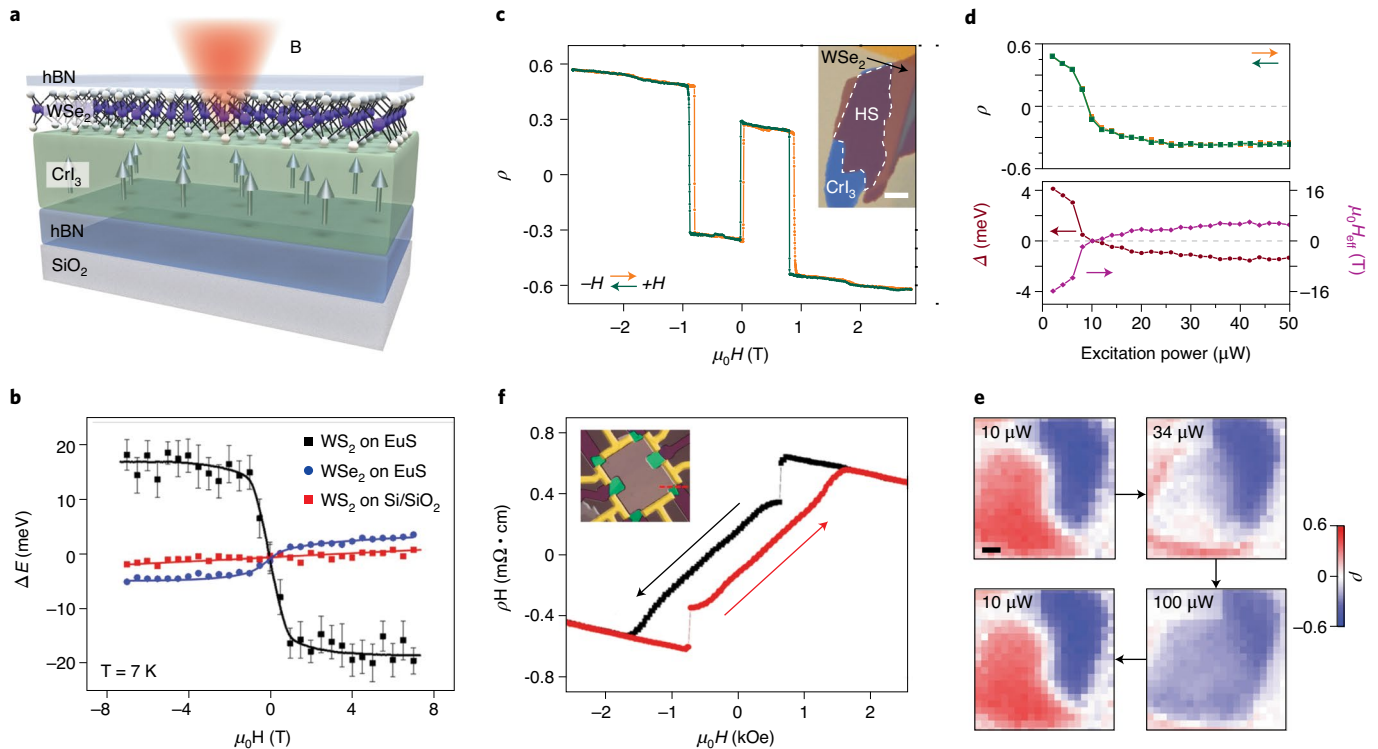


Fig. 6 | Magnetic proximity effects in vdW heterostructures. **a**, Schematic of a $\text{WSe}_2\text{-CrI}_3$ heterostructure. A monolayer of WSe_2 is interfaced with ultrathin CrI_3 (green) to induce magnetic proximity effects in the WSe_2 . The entire heterostructure is encapsulated by hBN to prevent degradation of the CrI_3 layer. **b**, Valley splitting of WS_2 (black) and WSe_2 (blue) monolayers on EuS as a function of magnetic field. This is juxtaposed with magnetic field-only valley splitting on nonmagnetic SiO_2 (red). Error bars represent one standard deviation in determining the Zeeman splitting. Solid lines are guides to the eye. **c**, Normalized intensity splitting between trion emission in the +K and -K valleys, ρ , in a $\text{WSe}_2\text{-CrI}_3$ heterostructure as a function of magnetic field. The inset shows a false-colour optical micrograph of an assembled $\text{WSe}_2\text{-CrI}_3$ heterostructure. The white dotted line delineates the heterostructure area. Scale bar, 3 μm . **d**, Excitation power-dependent ρ (top) and valley splitting (bottom, maroon), Δ , of a different $\text{WSe}_2\text{-CrI}_3$ heterostructure in a magnetic field of 0.88 T. Orange (green) curves represent ρ from data taken with increasing (decreasing) power. Extracted effective field induced by CrI_3 , $\mu_0 H_{\text{eff}}$, is also plotted in purple alongside Δ . Grey lines demarcate zero ρ , $\mu_0 H_{\text{eff}}$, and Δ . **e**, Spatial photoluminescence maps of the same heterostructure in **d** taken at 0.88 T with excitation powers in the sequence: 10 μW , 34 μW , 100 μW and 10 μW . Scale bar, 1 μm , the same size as the laser spot. Domains are visibly larger than the laser spot and can be switched to a different magnetic state by changing laser powers. **f**, Magnetic field-dependent proximitized anomalous Hall measurements of 5-nm-thick Pt layers in Pt-CrGeTe_3 heterostructures. Arrows indicate field sweep direction. A false-colour optical micrograph of the device is seen in the upper-left inset. Scale bar, 10 μm . Figure adapted with permission from: ref. ³⁶, AAAS (**a,c**); ref. ³², Springer Nature Ltd (**b**); ref. ³⁷, American Chemical Society (**d,e**); and ref. ¹²⁶, American Chemical Society (**f**).

metals like Pt and Pd, with magnetic proximity coupling observed in the metallic layer when interfaced with both magnetic insulators¹²⁴ and itinerant ferromagnets¹²⁵. In bilayer heterostructures of thin CrGeTe_3 flakes and 10-nm evaporated Pt films, shown in the inset of Fig. 6f, magnetic hysteresis is observed from anomalous Hall effect measurements of Pt (Fig. 6f), which disappears when heated above the T_C of CrGeTe_3 (ref. ¹²⁶). This, as well as calculations that show an induced moment in Pt from hybridization with Cr d orbitals confirm the imprinting of magnetic order on Pt from a 2D vdW magnetic insulator. Spin-orbit torque switching has also been recently realized in $\text{Fe}_3\text{GeTe}_2/\text{Pt}$ (refs. ^{34,127}) $\text{Fe}_3\text{GeTe}_2/\text{Ta}$ (ref. ¹²⁷) and $\text{CrGeTe}_3/\text{Ta}$ (ref. ³⁵), providing a new method to electrically switch the magnetization vector of ferromagnetic 2D materials.

The magnetic order of atomically thin vdW magnetic insulators can also be detected through lateral electrical transport when stacked on top of a graphene Hall cross³³. Using these graphene Hall bar micromagnetometers, the magnetic order of vdW magnetic insulators has been detected and their magnetic moment quantified down to the monolayer limit³³. For instance, ferromagnetism was observed in monolayer CrBr_3 and its magnetic moment was determined to be $\sim 3.6 \mu_B/\text{Cr}^{3+}$ at 2 K (ref. ³³). This is within reasonable agreement with the bulk CrBr_3 magnetic moment of $3.8 \mu_B/\text{Cr}^{3+}$

measured through SQUID in the same study³³, but surprisingly large compared to the expectations for trivalent Cr ($3.0 \mu_B$) and the reported saturation magnetization of bulk crystals ($2.85\text{--}3 \mu_B$)^{99,128}. These micromagnetometers were also able to detect magnetic hysteresis in CrGeTe_3 , though the detected stray field was not converted and compared to the expected magnetic moment per Cr^{2+} . One small caveat is that the applied magnetic field must be less than ~ 100 mT to ensure a cyclotron radius larger than the lateral dimensions of the Hall bar.

Outlook

In just the span of a few years, the field of magnetic vdW materials saw numerous advances and grew substantially to include several types of magnetic phases that can be controlled through external degrees of freedom such as electric fields and pressure, and leveraged through flexible heterostructure engineering. Device platforms, both new and revisited, have been realized using these magnetic 2D vdW heterostructures, of which this Review has only briefly surveyed.

One future direction is to further explore the interplay between magnetism and topology in twisted heterostructures. Skyrmions are topologically protected vortex-like magnetization textures that result from local variations of the magnetic exchange. Because the

interlayer exchange in layered vdW materials sensitively depends on the geometry of super-superexchange interactions, one can potentially observe skyrmions in a moiré superlattice by twisting two magnetic layers¹²⁹. Such moiré superlattices in magic-angle twisted bilayer graphene have led to a host of correlated states including ferromagnetism, giant anomalous Hall signal and chiral edge states at three-quarters filling of the conduction mini-band¹³⁰.

Another future prospect for magnetic vdW materials is their inclusion in vdW heterostructures for spintronics applications. In layered antiferromagnets, for instance, it would be ideal if one could electrically switch magnetic states without including a background magnetic field. This could potentially shift the spin-flip transition in the layered antiferromagnet closer to $B = 0$ T such that electrostatic doping can freely tune between the antiferromagnetic state and the fully spin-polarized state. Another option is through strain control of the magnetism in these magnetic vdW materials^{28,131}.

Despite these promising aspects, there are drawbacks which need to be addressed. Unlike most 2D magnetic systems, a majority of the vdW materials have magnetic ordering temperatures below room temperature and degrade in air; they are prone to oxidation (for example, CrGeTe_3 (refs. ^{14,62}) and Fe_3GeTe_2 (ref. ⁷³)) and hydration (CrI_3 (ref. ¹³²)). For practical applications using magnetic vdW heterostructures, air-stable, vdW materials that are magnetically ordered at ambient conditions need to be discovered, particularly magnetic insulators and semiconductors. This may require new vdW magnets with larger anisotropies and stronger exchange interactions in the monolayer limit. The recent discovery of itinerant ferromagnetism up to 270 K in ultrathin flakes of Fe_3GeTe_2 (ref. ⁵⁴) and at room temperature in monolayer MnSe_x (ref. ⁵³) and VSe_2 (ref. ⁵²) is a promising start for addressing this issue.

Received: 23 December 2019; Accepted: 30 July 2020;

Published online: 18 September 2020

References

- Novoselov, K. S. et al. Electric field effect in atomically thin carbon films. *Science* **306**, 666–669 (2004).
- Mak, K. F., Lee, C., Hone, J., Shan, J. & Heinz, T. F. Atomically thin MoS_2 : a new direct-gap semiconductor. *Phys. Rev. Lett.* **105**, 136805 (2010).
- Geim, A. K. & Grigorieva, I. V. Van der Waals heterostructures. *Nature* **499**, 419–425 (2013).
- Novoselov, K. S., Mishchenko, A., Carvalho, A. & Castro Neto, A. H. 2D materials and van der Waals heterostructures. *Science* **353**, aac9439 (2016).
- Baugher, B. W. H., Churchill, H. O. H., Yang, Y. & Jarillo-Herrero, P. Optoelectronic devices based on electrically tunable p-n diodes in a monolayer dichalcogenide. *Nat. Nanotechnol.* **9**, 262–267 (2014).
- Ross, J. S. et al. Electrically tunable excitonic light-emitting diodes based on monolayer WSe_2 p-n junctions. *Nat. Nanotechnol.* **9**, 268–272 (2014).
- Cheng, R. et al. Electroluminescence and photocurrent generation from atomically sharp $\text{WSe}_2/\text{MoS}_2$ heterojunction p-n diodes. *Nano Lett.* **14**, 5590–5597 (2014).
- Cao, Y. et al. Unconventional superconductivity in magic-angle graphene superlattices. *Nature* **556**, 43–50 (2018).
- Seyler, K. L. et al. Signatures of moiré-trapped valley excitons in $\text{MoSe}_2/\text{WSe}_2$ heterobilayers. *Nature* **567**, 66–70 (2019).
- Jin, C. et al. Observation of moiré excitons in WSe_2/WS_2 heterostructure superlattices. *Nature* **567**, 76–80 (2019).
- Tran, K. et al. Evidence for moiré excitons in van der Waals heterostructures. *Nature* **567**, 71–75 (2019).
- Alexeev, E. M. et al. Resonantly hybridized excitons in moiré superlattices in van der Waals heterostructures. *Nature* **567**, 81–86 (2019).
- Huang, B. et al. Layer-dependent ferromagnetism in a van der Waals Crystal down to the monolayer limit. *Nature* **546**, 270–273 (2017).
- Gong, C. et al. Discovery of intrinsic ferromagnetism in two-dimensional van der Waals crystals. *Nature* **546**, 265–269 (2017).
- De Jongh, L. J. Experiments on simple magnetic model systems. *J. Appl. Phys.* **49**, 1305–1310 (1978).
- Lines, M. E. Magnetism in two dimensions. *J. Appl. Phys.* **40**, 1352–1358 (1969).
- Cortie, D. L. et al. Two-dimensional magnets: forgotten history and recent progress towards spintronic applications. *Adv. Funct. Mater.* **2019**, 1901414 (2019).
- Vaz, C. A. F., Bland, J. A. C. & Lauhoff, G. Magnetism in ultrathin film structures. *Reports Prog. Phys.* **71**, 056501 (2008).
- Bhattacharya, A. & May, S. J. Magnetic oxide heterostructures. *Annu. Rev. Mater. Res.* **44**, 65–90 (2014).
- Scalapino, D. J. A common thread: the pairing interaction for unconventional superconductors. *Rev. Mod. Phys.* **84**, 1383–1417 (2012).
- Dai, P. Antiferromagnetic order and spin dynamics in iron-based superconductors. *Rev. Mod. Phys.* **87**, 855–896 (2015).
- Savary, L. & Balents, L. Quantum spin liquids: a review. *Reports Prog. Phys.* **80**, 016502 (2017).
- Burch, K. S., Mandrus, D. & Park, J. G. Magnetism in two-dimensional van der Waals materials. *Nature* **563**, 47–52 (2018).
- Gibertini, M., Koperski, M., Morpurgo, A. F. & Novoselov, K. S. Magnetic 2D materials and heterostructures. *Nat. Nanotechnol.* **14**, 408–419 (2019).
- Gong, C. & Zhang, X. Two-dimensional magnetic crystals and emergent heterostructure devices. *Science* **363**, eaav4450 (2019).
- Song, T. et al. Switching 2D magnetic states via pressure tuning of layer stacking. *Nat. Mater.* **18**, 1298–1302 (2019).
- Li, T. et al. Pressure-controlled interlayer magnetism in atomically thin CrI_3 . *Nat. Mater.* **18**, 1303–1308 (2019).
- Sivadas, N., Daniels, M. W., Swendsen, R. H., Okamoto, S. & Xiao, D. Magnetic ground state of semiconducting transition-metal trichalcogenide monolayers. *Phys. Rev. B* **91**, 235425 (2015).
- Cai, X. et al. Atomically thin CrCl_3 : an in-plane layered antiferromagnetic insulator. *Nano Lett.* **19**, 3993–3998 (2019).
- Kim, H. H. et al. Evolution of interlayer and intralayer magnetism in three atomically thin chromium trihalides. *Proc. Natl Acad. Sci. USA* **116**, 11131–11136 (2019).
- Klein, D. R. et al. Enhancement of interlayer exchange in an ultrathin two-dimensional magnet. *Nat. Phys.* **15**, 1255–1260 (2019).
- Norden, T. et al. Giant valley splitting in monolayer WS_2 by magnetic proximity effect. *Nat. Commun.* **10**, 4163 (2019).
- Kim, M. et al. Hall micromagnetometry of individual two-dimensional ferromagnets. *Nat. Electron.* **2**, 457–463 (2019).
- Alghamdi, M. et al. Highly efficient spin-orbit torque and switching of layered ferromagnet Fe_3GeTe_2 . *Nano Lett.* **19**, 4400–4405 (2019).
- Ostwal, V., Shen, T. & Appenzeller, J. Efficient spin-orbit torque switching of the semiconducting van der Waals ferromagnet $\text{Cr}_2\text{Ge}_2\text{Te}_6$. *Adv. Mater.* **32**, 1906021 (2020).
- Zhong, D. et al. Van der Waals engineering of ferromagnetic semiconductor heterostructures for spin and valleytronics. *Sci. Adv.* **3**, e1603113 (2017).
- Seyler, K. L. et al. Valley manipulation by optically tuning the magnetic proximity effect in $\text{WSe}_2/\text{CrI}_3$ heterostructures. *Nano Lett.* **18**, 3823–3828 (2018).
- Otrokov, M. M. et al. Prediction and observation of an antiferromagnetic topological insulator. *Nature* **576**, 416–422 (2019).
- Liu, C. et al. Quantum phase transition from axion insulator to Chern insulator in MnBi_2Te_4 . *Nat. Mater.* **19**, 522–527 (2020).
- Brec, R. Review on structural and chemical properties of transition metal phosphorous trisulfides MPS_3 . *Solid State Ion.* **22**, 3–30 (1986).
- Kim, K. et al. Suppression of magnetic ordering in XXZ -type antiferromagnetic monolayer NiPS_3 . *Nat. Commun.* **10**, 345 (2019).
- Kim, K. et al. Antiferromagnetic ordering in van der Waals 2D magnetic material MnPS_3 probed by Raman spectroscopy. *2D Mater.* **6**, 041001 (2019).
- Sun, Y. J., Tan, Q. H., Liu, X. L., Gao, Y. F. & Zhang, J. Probing the magnetic ordering of antiferromagnetic MnPS_3 by Raman spectroscopy. *J. Phys. Chem. Lett.* **10**, 3087–3093 (2019).
- Susner, M. A., Chyashvichyus, M., McGuire, M. A., Ganesh, P. & Maksymovych, P. Metal thio- and selenophosphates as multifunctional van der Waals layered materials. *Adv. Mater.* **29**, 1602852 (2017).
- Jernberg, P., Bjarman, S. & Wäppling, R. FePS_3 : a first-order phase transition in a '2D' Ising antiferromagnet. *J. Magn. Magn. Mater.* **46**, 178–190 (1984).
- Rule, K. C., McIntyre, G. J., Kennedy, S. J. & Hicks, T. J. Single-crystal and powder neutron diffraction experiments on FePS_3 : search for the magnetic structure. *Phys. Rev. B* **76**, 134402 (2007).
- Wildes, A. R. et al. Magnetic structure of the quasi-two-dimensional antiferromagnet NiPS_3 . *Phys. Rev. B* **92**, 224408 (2015).
- Joy, P. A. & Vasudevan, S. Magnetism in the layered transition-metal thiophosphates MPS_3 ($M = \text{Mn, Fe, and Ni}$). *Phys. Rev. B* **46**, 5425–5433 (1992).
- Lançon, D., Ewings, R. A., Guidi, T., Formisano, F. & Wildes, A. R. Magnetic exchange parameters and anisotropy of the quasi-two-dimensional antiferromagnet NiPS_3 . *Phys. Rev. B* **98**, 134414 (2018).
- Lee, J. U. et al. Ising-type magnetic ordering in atomically thin FePS_3 . *Nano Lett.* **16**, 7433–7438 (2016).
- McCreary, A. et al. Quasi-two-dimensional magnon identification in antiferromagnetic FePS_3 via magneto-Raman spectroscopy. *Phys. Rev. B* **101**, 064416 (2020).

52. Bonilla, M. et al. Strong room-temperature ferromagnetism in VSe_2 monolayers on van der Waals substrates. *Nat. Nanotechnol.* **13**, 289–293 (2018).
53. O'Hara, D. J. et al. Room temperature intrinsic ferromagnetism in epitaxial manganese selenide films in the monolayer limit. *Nano Lett.* **18**, 3125–3131 (2018).
54. May, A. F. et al. Ferromagnetism near room temperature in the cleavable van der Waals crystal Fe_3GeTe_2 . *ACS Nano* **13**, 4436–4442 (2019).
55. Yan, J. Q. et al. Crystal growth and magnetic structure of $MnBi_2Te_4$. *Phys. Rev. Mater.* **3**, 064202 (2019).
56. Chen, B. et al. Intrinsic magnetic topological insulator phases in the Sb doped $MnBi_2Te_4$ bulks and thin flakes. *Nat. Commun.* **10**, 4469 (2019).
57. Wu, J. et al. Natural van der Waals heterostructures with tunable magnetic and topological states. *Sci. Adv.* **5**, eaax9989 (2019).
58. Otrokov, M. M. et al. Unique thickness-dependent properties of the van der Waals interlayer antiferromagnet $MnBi_2Te_4$ films. *Phys. Rev. Lett.* **122**, 107202 (2019).
59. Deng, Y. et al. Quantum anomalous Hall effect in intrinsic magnetic topological insulator $MnBi_2Te_4$. *Science* **367**, 895–900 (2020).
60. Ge, J. et al. High-charge-number and high-temperature quantum hall effect without Landau levels. *Natl. Sci. Rev.* <https://doi.org/10.1093/nsr/nwaa089> (2020).
61. Carreaux, V., Brunet, D., Ouyard, G. & Andre, G. Crystallographic, magnetic and electronic structures of a new layered ferromagnetic compound $Cr_2Ge_2Te_6$. *J. Phys. Condens. Matter* **7**, 69–87 (1995).
62. Tian, Y., Gray, M. J., Ji, H., Cava, R. J. & Burch, K. S. Magneto-elastic coupling in a potential ferromagnetic 2D atomic crystal. *2D Mater.* **3**, 025035 (2016).
63. Wang, Z. et al. Electric-field control of magnetism in a few-layered van der Waals ferromagnetic semiconductor. *Nat. Nanotechnol.* **13**, 554–559 (2018).
64. Chen, B. et al. Magnetic properties of layered itinerant electron ferromagnet Fe_3GeTe_2 . *J. Phys. Soc. Japan* **82**, 124711 (2013).
65. Yi, J. et al. Competing antiferromagnetism in a quasi-2D itinerant ferromagnet: Fe_3GeTe_2 . *2D Mater.* **4**, 011005 (2016).
66. Deiseroth, H. J., Aleksandrov, K., Reiner, C., Kienle, L. & Kremer, R. K. Fe_3GeTe_2 and Ni_3GeTe_2 - two new layered transition-metal compounds: Crystal structures, HRTEM investigations, and magnetic and electrical properties. *Eur. J. Inorg. Chem.* **2006**, 1561–1567 (2006).
67. Tan, C. et al. Hard magnetic properties in nanoflake van der Waals Fe_3GeTe_2 . *Nat. Commun.* **9**, 1554 (2018).
68. May, A. F., Calder, S., Cantoni, C., Cao, H. & McGuire, M. A. Magnetic structure and phase stability of the van der Waals bonded ferromagnet $Fe_{3-x}GeTe_x$. *Phys. Rev. B* **93**, 014411 (2016).
69. Desai, S. B. et al. Gold-mediated exfoliation of ultralarge optoelectronically-perfect monolayers. *Adv. Mater.* **28**, 4053–4058 (2016).
70. Velický, M. et al. Mechanism of gold-assisted exfoliation of centimeter-sized transition-metal dichalcogenide monolayers. *ACS Nano* **12**, 10463–10472 (2018).
71. Magda, G. Z. et al. Exfoliation of large-area transition metal chalcogenide single layers. *Sci. Rep.* **5**, 14714 (2015).
72. Deng, Y. et al. Gate-tunable room-temperature ferromagnetism in two-dimensional Fe_3GeTe_2 . *Nature* **563**, 94–99 (2018).
73. Fei, Z. et al. Two-dimensional itinerant ferromagnetism in atomically thin Fe_3GeTe_2 . *Nat. Mater.* **17**, 778–782 (2018).
74. Liu, S. et al. Wafer-scale two-dimensional ferromagnetic Fe_3GeTe_2 thin films were grown by molecular beam epitaxy. *npj 2D Mater. Appl.* **1**, 30 (2017).
75. Weber, D., Trout, A. H., McComb, D. W. & Goldberger, J. E. Decomposition-induced room-temperature magnetism of the Na-intercalated layered ferromagnet $Fe_{3-x}GeTe_x$. *Nano Lett.* **19**, 5031–5035 (2019).
76. van Bruggen, C. F. & Haas, C. Magnetic susceptibility and electrical properties of VSe_2 single crystals. *Solid State Commun.* **20**, 251–254 (1976).
77. Bayard, M. & Sienko, M. J. Anomalous electrical and magnetic properties of vanadium diselenide. *J. Solid State Chem.* **19**, 325–329 (1976).
78. Onari, S. & Arai, T. Infrared lattice vibrations and dielectric dispersion in antiferromagnetic semiconductor $MnSe_2$. *J. Phys. Soc. Japan* **46**, 184–188 (1979).
79. Pollard, R. J., McCann, V. H. & Ward, J. B. Magnetic structures of α -MnS and MnSe from ^{57}Fe Mossbauer spectroscopy. *J. Phys. C Solid State Phys.* **16**, 345–353 (1983).
80. Duvjir, G. et al. Emergence of a metal-insulator transition and high-temperature charge-density waves in VSe_2 at the monolayer limit. *Nano Lett.* **18**, 5432–5438 (2018).
81. Ma, Y. et al. Evidence of the existence of magnetism in pristine VX_2 monolayers ($X = S, Se$) and their strain-induced tunable magnetic properties. *ACS Nano* **6**, 1695–1701 (2012).
82. Kan, M., Adhikari, S. & Sun, Q. Ferromagnetism in MnX_2 ($X = S, Se$) monolayers. *Phys. Chem. Chem. Phys.* **16**, 4990–4994 (2014).
83. Fumega, A. O. et al. Absence of ferromagnetism in VSe_2 caused by its charge density wave phase. *J. Phys. Chem. C* **123**, 27802–27810 (2019).
84. Coelho, P. et al. Charge density wave state suppresses ferromagnetic ordering in VSe_2 monolayers. *J. Phys. Chem. C* **123**, 14089–14096 (2019).
85. Lado, J. L. & Fernández-Rossier, J. On the origin of magnetic anisotropy in two dimensional CrI_3 . *2D Mater.* **4**, 035002 (2017).
86. Wong, P. K. J. et al. Evidence of spin frustration in a vanadium diselenide monolayer magnet. *Adv. Mater.* **31**, 1901185 (2019).
87. Feng, J. et al. Electronic structure and enhanced charge-density wave order of monolayer VSe_2 . *Nano Lett.* **18**, 4493–4499 (2018).
88. Kong, T. et al. VI_3 - a new layered ferromagnetic semiconductor. *Adv. Mater.* **31**, 1808074 (2019).
89. Tian, S. et al. Ferromagnetic van der Waals Crystal VI_3 . *J. Am. Chem. Soc.* **141**, 5326–5333 (2019).
90. Son, S. et al. Bulk properties of the van der Waals hard ferromagnet VI_3 . *Phys. Rev. B* **99**, 041402 (2019).
91. Balents, L. Spin liquids in frustrated magnets. *Nature* **464**, 199–208 (2010).
92. Zhang, W. B., Qu, Q., Zhu, P. & Lam, C. H. Robust intrinsic ferromagnetism and half semiconductivity in stable two-dimensional single-layer chromium trihalides. *J. Mater. Chem. C* **3**, 12457–12468 (2015).
93. McGuire, M. A., Dixit, H., Cooper, V. R. & Sales, B. C. Coupling of crystal structure and magnetism in the layered, ferromagnetic insulator CrI_3 . *Chem. Mater.* **27**, 612–620 (2015).
94. Morosin, B. & Narath, A. X-ray diffraction and nuclear quadrupole resonance studies of chromium trichloride. *J. Chem. Phys.* **40**, 1958–1967 (1964).
95. McGuire, M. A. et al. Magnetic behavior and spin-lattice coupling in cleavable van der Waals layered $CrCl_3$ crystals. *Phys. Rev. Mater.* **1**, 014001 (2017).
96. Wang, H., Fan, F., Zhu, S. & Wu, H. Doping enhanced ferromagnetism and induced half-metallicity in CrI_3 monolayer. *Europhys. Lett.* **114**, 47001 (2016).
97. Kanamori, J. Superexchange interaction and symmetry properties of electron orbitals. *J. Phys. Chem. Solids* **10**, 87–98 (1959).
98. Hansen, W. N. Some magnetic properties of the chromium (III) halides at 4.2°K. *J. Appl. Phys.* **30**, 304S–305S (1959).
99. Tsubokawa, I. On the magnetic properties of a $CrBr_3$ single crystal. *J. Phys. Soc. Japan* **15**, 1664–1668 (1960).
100. Narath, A. Low-temperature sublattice magnetization of antiferromagnetic $CrCl_3$. *Phys. Rev.* **131**, 1929–1942 (1963).
101. Narath, A. & Davis, H. L. Spin-wave analysis of the sublattice magnetization behavior of antiferromagnetic and ferromagnetic $CrCl_3$. *Phys. Rev.* **137**, A163–A178 (1965).
102. Kuhlow, B. Magnetic ordering in $CrCl_3$ at the phase transition. *Phys. Status Solidi* **72**, 161–168 (1982).
103. Bené, R. W. Electron-paramagnetic-resonance study of Cr ions and exchange-coupled Cr ion pairs in the BiI_3 structure. *Phys. Rev.* **178**, 497–513 (1969).
104. Abramchuk, M. et al. Controlling magnetic and optical properties of the van der Waals crystal $CrCl_{3-x}Br_x$ via mixed halide chemistry. *Adv. Mater.* **30**, 1801325 (2018).
105. Wu, M., Li, Z., Cao, T. & Louie, S. G. Physical origin of giant excitonic and magneto-optical responses in two-dimensional ferromagnetic insulators. *Nat. Commun.* **10**, 2371 (2019).
106. Song, T. et al. Giant tunneling magnetoresistance in spin-filter van der Waals heterostructures. *Science* **360**, 1214–1218 (2018).
107. Hellwig, O., Berger, A., Kortright, J. B. & Fullerton, E. E. Domain structure and magnetization reversal of antiferromagnetically coupled perpendicular anisotropy films. *J. Magn. Magn. Mater.* **319**, 13–55 (2007).
108. Chen, B. et al. All-oxide-based synthetic antiferromagnets exhibiting layer-resolved magnetization reversal. *Science* **357**, 191–194 (2017).
109. Thiel, L. et al. Probing magnetism in 2D materials at the nanoscale with single spin microscopy. *Science* **364**, 973–976 (2019).
110. Sun, Z. et al. Giant nonreciprocal second-harmonic generation from antiferromagnetic bilayer CrI_3 . *Nature* **572**, 497–501 (2019).
111. Seyler, K. L. et al. Ligand-field helical luminescence in a 2D ferromagnetic insulator. *Nat. Phys.* **14**, 277–281 (2018).
112. Zhang, Z. et al. Direct photoluminescence probing of ferromagnetism in monolayer two-dimensional $CrBr_3$. *Nano Lett.* **19**, 3138–3142 (2019).
113. Jagla, E. A. Hysteresis loops of magnetic thin films with perpendicular anisotropy. *Phys. Rev. B* **72**, 094406 (2005).
114. Jiang, P. et al. Stacking tunable interlayer magnetism in bilayer CrI_3 . *Phys. Rev. B* **99**, 144401 (2019).
115. Goodenough, J. B. Theory of the role of covalence in the perovskite-type manganites $[La, M(II)]MnO_3$. *Phys. Rev.* **100**, 564–573 (1955).
116. Ubrig, N. et al. Low-temperature monoclinic layer stacking in atomically thin CrI_3 crystals. *2D Mater.* **7**, 015007 (2020).
117. Sivadas, N., Okamoto, S., Xu, X., Fennie, C. J. & Xiao, D. Stacking-dependent magnetism in bilayer CrI_3 . *Nano Lett.* **18**, 7658–7664 (2018).
118. MacNeill, D. et al. Gigahertz frequency antiferromagnetic resonance and strong magnon-magnon coupling in the layered crystal $CrCl_3$. *Phys. Rev. Lett.* **123**, 047204 (2019).
119. Chen, W. et al. Direct observation of van der Waals stacking-dependent interlayer magnetism. *Science* **366**, 983–987 (2019).

120. Manzeli, S., Ovchinnikov, D., Pasquier, D., Yazyev, O. V. & Kis, A. 2D transition metal dichalcogenides. *Nat. Rev. Mater.* **2**, 17033 (2017).
121. Cai, T. et al. Magnetic control of the valley degree of freedom of massive Dirac fermions with application to transition metal dichalcogenides. *Phys. Rev. B* **88**, 115140 (2013).
122. Stier, A. V. et al. Magneto-optics of exciton Rydberg states in a monolayer semiconductor. *Phys. Rev. Lett.* **120**, 057406 (2018).
123. Aivazian, G. et al. Magnetic control of valley pseudospin in monolayer WSe₂. *Nat. Phys.* **11**, 148–152 (2015).
124. Huang, S. Y. et al. Transport magnetic proximity effects in platinum. *Phys. Rev. Lett.* **109**, 107204 (2012).
125. Hellman, F. et al. Interface-induced phenomena in magnetism. *Rev. Mod. Phys.* **89**, 025006 (2017).
126. Lohmann, M. et al. Probing magnetism in insulating Cr₂Ge₂Te₆ by induced anomalous Hall effect in Pt. *Nano Lett.* **19**, 2397–2403 (2019).
127. Wang, X. et al. Current-driven magnetization switching in a van der Waals ferromagnet Fe₃GeTe₂. *Sci. Adv.* **5**, eaaw8904 (2019).
128. Yu, X. et al. Large magnetocaloric effect in van der Waals crystal CrBr₃. *Front. Phys.* **14**, 6–10 (2019).
129. Tong, Q., Liu, F., Xiao, J. & Yao, W. Skyrmions in the moiré of van der Waals 2D magnets. *Nano Lett.* **18**, 7194–7199 (2018).
130. Sharpe, A. L. et al. Emergent ferromagnetism near three-quarters filling in twisted bilayer graphene. *Science* **365**, 605–608 (2019).
131. Wu, Z., Yu, J. & Yuan, S. Strain-tunable magnetic and electronic properties of monolayer CrI₃. *Phys. Chem. Chem. Phys.* **21**, 7750–7755 (2019).
132. Shcherbakov, D. et al. Raman spectroscopy, photocatalytic degradation, and stabilization of atomically thin chromium tri-iodide. *Nano Lett.* **18**, 4214–4219 (2018).
133. Huang, B. et al. Tuning inelastic light scattering via symmetry control in the two-dimensional magnet CrI₃. *Nat. Nanotechnol.* **15**, 212–216 (2020).
134. Wiesendanger, R. Spin mapping at the nanoscale and atomic scale. *Rev. Mod. Phys.* **81**, 1495–1550 (2009).
135. Schirhagl, R., Chang, K., Loretz, M. & Degen, C. L. Nitrogen-vacancy centers in diamond: nanoscale sensors for physics and biology. *Annu. Rev. Phys. Chem.* **65**, 83–105 (2014).
136. Degen, C. L. Scanning magnetic field microscope with a diamond single-spin sensor. *Appl. Phys. Lett.* **92**, 243111 (2008).
137. Casola, F., Van Der Sar, T. & Yacoby, A. Probing condensed matter physics with magnetometry based on nitrogen-vacancy centres in diamond. *Nat. Rev. Mater.* **3**, 17088 (2018).

Acknowledgements

The authors acknowledge D. Klein, Q. Zhang and D. Ovchinnikov for constructive feedback. The work at the University of Washington is mainly supported by the Department of Energy, Basic Energy Sciences, Materials Sciences and Engineering Division (DE-SC0018171 and DE-SC0012509). M.A.M. and A.M. were supported by the US Department of Energy, Office of Science, Basic Energy Sciences, Materials Sciences and Engineering Division. Work at MIT was mainly supported by the DOE Office of Science, Basic Energy Sciences under award DE-SC0018935, the Center for Integrated Quantum Materials under NSF grant DMR-1231319, as well as the Gordon and Betty Moore Foundation's EPIQS Initiative through grant GBMF4541 to P.J.H. D.X., P.J.H. and X.X. acknowledge partial support from Air Force Office of Scientific Research (AFOSR) 2D MAGIC MURI FA9550-19-1-0390.

Author contributions

The experimental and theoretical work reviewed here has been performed largely by the co-authors and their groups. B.H. and X.X. led the writing of this manuscript, with input from all co-authors.

Competing interests

The authors declare no competing interests.

Additional information

Correspondence should be addressed to B.H. or X.X.

Reprints and permissions information is available at www.nature.com/reprints.

Publisher's note Springer Nature remains neutral with regard to jurisdictional claims in published maps and institutional affiliations.

© Springer Nature Limited 2020